Morphological Considerations in Templated Porous Ag Catalysts for Electrochemical CO_2 Reduction

Karen van den Akker

Materials Chemistry and Catalysis
Utrecht University
Netherlands

November 2021 - March 2023

Daily supervisor: Maaike van Ittersum, MSc
Examined by prof. dr. Petra de Jongh and dr. Peter Ngene

A thesis presented for the degree of Master of Science

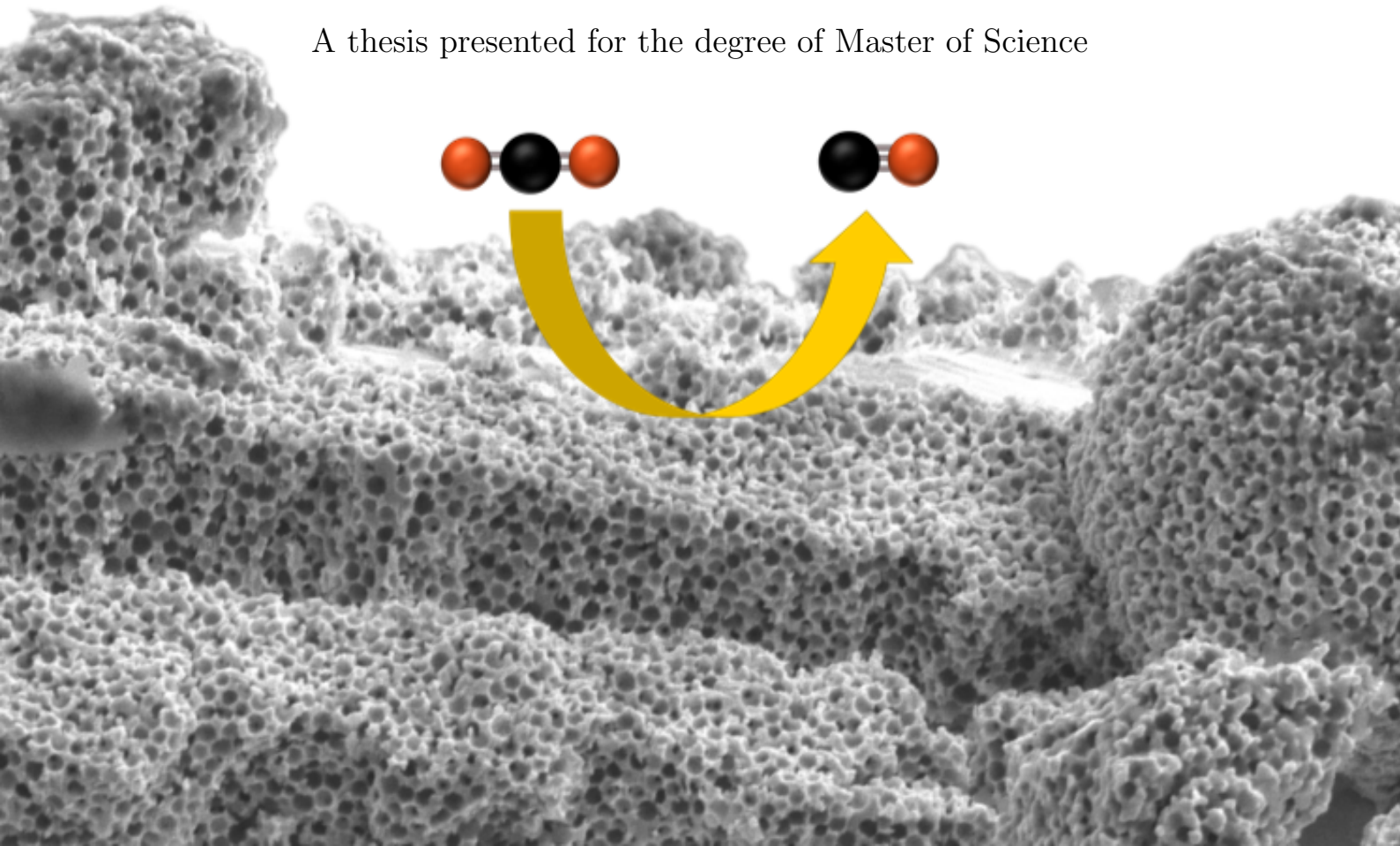

Abstract

Electrochemical reduction of CO_2 using renewable electricity is a promising strategy to produce fuels and chemical feedstocks while simultaneously decreasing greenhouse gas emissions. Porous Ag catalysts are reported to have a high CO selectivity and activity, but the complex combination of porosity and morphology makes it hard to gain a full understanding of CO_2 reduction in porous metals. In order to study the effect of morphology variations in porous Ag, a template-based electrodeposition route was developed. In addition, the effect of porosity was established by comparing porous Ag to non-porous Ag.

Electrodeposition parameters were varied to control the morphology of porous and non-porous Ag. Porous Ag consistently reached higher CO partial current density values, 3.45 - 4.25 mA/cm^2, compared to non-porous Ag, 2.21 - 2.97 mA/cm^2, at -1.4 V vs RHE. We demonstrated that only for certain Ag morphologies, porous samples reached higher CO and lower H_2 faradaic efficiencies compared to their non-porous counterpart. In combination with the absence of porosity-induced suppression of the hydrogen evolution reaction in coral-like porous structures, this indicated that the morphology surrounding porosity contributes significantly to the catalytic performance. Therefore, this study establishes that porosity enhances CO_2 to CO conversion, while simultaneously highlighting the importance of additional morphological considerations.

Contents

List of Figures

List of Tables

List of Abbreviations

A	Surface area
F	Factor by which surface area increases as a result of porosity
I	Current
j_{CO}	CO partial current density
j_{H_2}	H_2 partial current density
j_{tot}	Total current density
CA	Chronoamperometry
CV	Cyclic voltammetry
DLC	Double layer capacitance
ECSA	Electrochemical surface area
EDX	Energy dispersive X-ray spectroscopy
FE	Faradaic efficiency
GC	Gas chromotography
HER	Hydrogen evolution reaction
HR-SEM	High resolution scanning electron microscopy
NHE	Normal hydrogen electrode
NMR	Nuclear magnetic resonance spectroscopy
PMMA	Poly(methyl methacrylate)
PS	Polystyrene
RHE	Reversible hydrogen electrode

Chapter 1

Introduction

Weather and climate extremes in every region of the world have already been affected by the current anthropogenic global warming of 1°C, according to the Intergovernmental Panel on Climate Change.[1] Only if CO_2 emissions are extensively reduced in the next couple of decades, global warming will not exceed 1.5 °C and 2 °C in the 21st century.[1] Accordingly, it is urgent to replace fossil fuels with more sustainable resources for fulfilling energy and chemical feedstock demands.[2–4] Electrochemical CO_2 reduction powered by renewable energy offers the potential to close the carbon cycle while producing high-value chemical compounds.[2,5–7] Other characteristics of electrochemical CO_2 reduction that make it favorable for large-scale implementation, include the ambient reaction conditions and facile control of the reaction rate.[3,8]

Great challenges for CO_2 reduction still remain, such as overcoming the high energy barrier of dissociation of the C=O bond. Difficulties are also encountered when navigating between the great range of complicated proton-assisted reactions that occur at similar potentials and result in different products, reducing the selectivity.[3,4] Therefore, the design of an electrocatalyst with high stability, activity, and selectivity towards the desired products at low overpotentials is crucial.[2–5,8]

Ag is a promising candidate as a catalyst for CO_2 reduction, as it has a high activity and high CO selectivity. CO is a valuable product because when used as a feedstock in existing Fischer-Tropsch processes, it can be further converted into fuels and other chemical feedstocks. In addition, Ag is cheaper and more abundant than Au, a different monometallic catalyst with high CO selectivity.[9,10]

Another crucial means of control over the catalytic performance is the catalyst morphology.[11,12] This can be divided into multiple aspects. For instance, the ratio of crystal facets can highly impact the catalyst performance. In the case of silver, the Ag(110) site has been found to have the highest selectivity towards electroreduction of CO_2 to CO.[12,13] In addition, increasing the effective surface area of the catalyst boosts the number of available active sites.[11,12] When this is achieved by introducing porosity in the catalyst, the bulk nature of the material facilitates electron transfer and inhibits Ostwald ripening.[14]

Several strategies have been used to create porous Ag catalyst for CO_2 reduction. For example, nanoporous Ag was prepared by Lu et al. via the dealloying of Ag-Al with HCl, and Wang et al. used dynamic hydrogen bubble templating.[9,15] The promising electrocatalytic performance of the porous catalysts was attributed to the high surface area and the presence of curved edges with a high number of uncoordinated atoms. In addition, mass-transport conditions in porous structures

likely greatly affect the local concentrations of various active species, such as CO_2 and H^+, and hence the catalytic performance, as is reported for porous Au catalysts.[16] However, the methods to introduce porosity presented in literature, have limited control over the morphology and pore structure, which makes it hard to distinguish the contributing factors.

In order to gain a deeper fundamental understanding of porosity effects in Ag catalysts, it is therefore important to use well-defined porous Ag model catalysts. This can be achieved by using a hard templating strategy. Specifically, colloidal crystals from PS or PMMA are promising sacrificial templates, as they can be highly ordered and facilitate control of pore shape and size. Even greater control over the electrode morphology can be realized by merging the templating strategy with electrodeposition. With electrodeposition, fine control over surface morphology is possible by the inclusion of complexing agents, deposition potential, and current as parameters.[17–20] Moreover, it allows the facile production of a surfactant-free material with an electronically conductive surface, as required for electrocatalysis.[21,22] Finally, the strategy is suitable for large-scale implementation due to its low costs and solution-based operation under ambient conditions.[17,21,22]

To this date, only one model system of porous Ag for electrochemical CO_2 reduction has been prepared via a similar approach. Yoon et al. synthesized a highly ordered mesoporous silver inverse opal (Ag-IO), using a sacrificial PS colloidal crystal template. They reported that the mesoporosity suppressed H_2 formation while simultaneously promoting the CO_2 to CO conversion.[23] However, the effect of introducing porosity in different Ag morphologies is yet to be explored.

Therefore, the aim of this study was to develop template-based porous Ag catalysts and investigate how the porosity and the structure surrounding the pores relate to the catalytic performance for CO_2 reduction. Herein, we fabricated porous and non-porous Ag electrocatalysts on Ag foil under different electrodeposition conditions using a sacrificial PMMA sphere template and determined their performance in electrochemical CO_2 reduction. In addition, we performed exploratory research on porous Ag-Cu. These obtained results will contribute to a deeper fundamental understanding of porous catalysts for CO_2 reduction.

Chapter 2

Theory

This chapter contains the theoretical background for this thesis. First, an introduction to electrochemistry is presented, followed by an overview of electrochemical CO_2 reduction. Finally, the synthesis of porous silver will be discussed.

2.1 Electrochemistry

Electrochemistry involves reactions with electron transfers between an electrode surface and molecules. This means that the current is directly related to the reaction rate. Since the current (I) depends on the electrode surface area (A), a more fundamental descriptor of the rate is the current density ($j = I/A$).[24] The energy of the electrons is controlled by applying a potential. For a non-spontaneous electrochemical reduction reaction, electron transfer will occur when the energy of electrons in the electrode is higher than the LUMO of the to-be-reduced species. The driving force for the reaction is the difference in energy between the electrode electrons and the LUMO of the species. Therefore, the driving force can be easily controlled with the applied potential. Accordingly, the current density also depends on the applied potential.[25] In order to be able to apply a potential, non-spontaneous electrochemical reactions are carried out in an electrochemical cell. A more detailed account of electrochemical cells is provided in the section below. This will be followed by an explanation of electrochemical techniques that can be used to assess electrocatalysts and an introduction to the terms that are used to express the electrochemical performance.

2.1.1 Electrochemical cell

As briefly mentioned above, electrochemical reduction reactions take place in an electrochemical cell. There are multiple types of electrochemical cells, but here the focus will be on the use of the most common H-type cell.[26] An H-type cell, as illustrated in Figure 2.1, consists of an anodic and a cathodic compartment, both connected to a potentiostat. These compartments are filled with an electrolyte solution and separated by an ion exchange membrane. This prevents oxidation of reduced species, while simultaneously enabling complete charge neutrality. For reduction reactions, the working electrode and a reference electrode are set in the cathodic compartment. The anodic side then contains a counter electrode, such as Pt, that completes the electron circuit.[24,26]

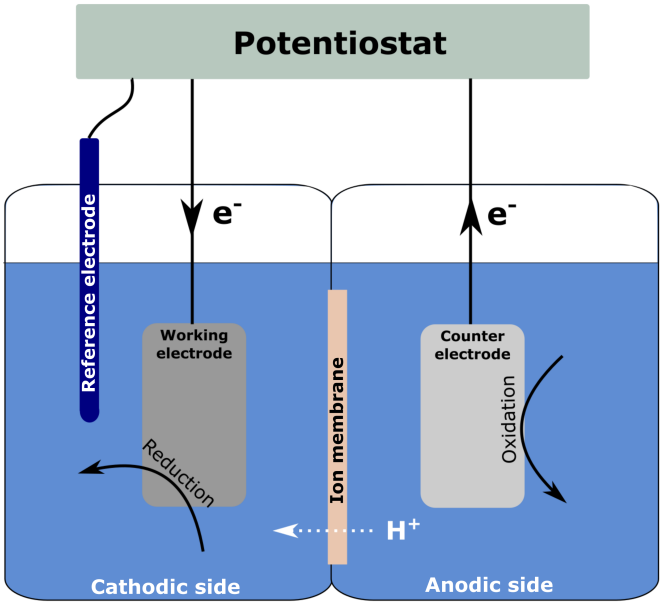

Figure 2.1: Schematic representation of an H-type cell. The cathodic side contains the working electrode, where reduction takes place and a reference electrode. Oxidation on the counter electrode at the anodic side completes the electron circuit. An ion exchange membrane between the two compartments facilitates ion transport.

2.1.2 Electrochemical techniques

Having explained what an electrochemical cel consists of, it is time to discuss the measurements that can be conducted in it. In this work, several electrochemical techniques are utilized, such as cyclic voltammetry (CV), double layer capacitance (DLC), and chronoamperometry. Each will be discussed in turn.

2.1.2.1 Cyclic voltammetry

During CV the current is measured as a function of the applied potential. The potential is for example first linearly decreased to probe cathodic reactions and then linearly increased until the starting potential is reached again. With this method, the faradaic processes are examined, so it provides a deeper understanding of the occurring oxidation and reduction reactions within a selected potential window.

An important parameter for this measurement is the rate at which the potential is changed, the scan rate. At the electrode surface, the concentration of electroactive species is depleted during the reduction reaction. This implies that the local concentration at the electrode surface is different from the bulk concentration, leading to a concentration gradient. This gradient is a driving force for diffusion, with larger gradients generating faster diffusion and subsequently an increased measured current. When a faster scan rate is used, relatively less time is available for the depletion of the electroactive species near the electrode surface. This results in a steeper concentration gradient and ultimately a greater current.[25,27,28]

2.1.2.2 Double layer capacitance

DLC measurements can be used to probe the electrochemical surface area (ECSA) of an electrocatalyst. The ECSA is described by

$$ECSA = \frac{C_{\mathrm{DL}}}{C_{\mathrm{S}}}, \tag{2.1}$$

where C_{DL} is the double layer capacitance, and C_{s} is the specific capacitance of the catalyst material. Since C_{s} is generally unknown, it is common practice to use an arbitrary value. This can result in a large underestimation or overestimation of the ECSA.[29] However, the ECSA is still a powerful tool to compare electrocatalysts of the same material. $\mathrm{C_{DL}}$ is determined with scan rate dependent cyclic voltammetry measurements in a narrow, non-faradaic potential region.[29,30] In this region, the steady state capacitive current i_{c} is proportional to the scan rate v and capacitance C for an ideal capacitor.

$$i_{\mathrm{c}} = v \cdot C \tag{2.2}$$

Therefore, the slope of a plot of i_{c} against the scan rates corresponds to C_{DL}.

2.1.2.3 Chronoamperometry

During a chronoamperometry (CA) measurement, the applied potential is fixed, and the resulting current is measured as a function of time. When coupled with gas chromatography, and nuclear magnetic resonance spectroscopy for liquid products, this technique can provide information about the catalytic performance.

2.1.3 Electrochemical performance

With the techniques described above, the electrochemical performance of a catalyst can be determined. There are several terms that are commonly used to define electrocatalytic performance, such as the faradaic efficiency, partial current density and onset potential. The selectivity of an electrocatalyst is often expressed as the faradaic efficiency (FE). The FE shows the percentage of electrons used for the formation of a specific product, and it can be calculated via

$$FE = \frac{\nu F n}{It} * 100\%. \tag{2.3}$$

Here, ν is the number of moles of electrons necessary for one mole of product and F is the Faraday constant. The total amount of product formed in moles is indicated by n. I represents the average current and t is the time of the measurement in seconds.

When $\mathrm{FE_{product}}$ is multiplied with the total current density j_{tot}, which is a measure of the electron transfer rate (Section 2.1), the partial current density j_{product} is obtained. This shows the activity of a catalyst towards a certain product.

Another term that is used to define the catalytic performance is the onset potential. The definition of onset potential varies between studies, but it is generally perceived as the potential at which the faradaic process of interest starts.[31] In literature, several ways are employed to determine the onset potential. Most frequently, a set threshold current value is selected, and the potential where the current reaches that value corresponds to the onset potential. However, these threshold values differ

greatly amongst different studies (10 µA - 10 mA). Therefore, it is not a suitable quantity for inter-study comparisons, but it can be employed in a single study. However, it is important to realize that the current is dependent on the surface area. This implies that catalysts with a higher ECSA will inherently reach threshold currents at lower potentials.[31]

2.2 Electrochemical CO_2 reduction

In this section the electrochemical reduction of CO_2 will be discussed in more detail. First, a possible mechanism of the reaction of interest is provided, and then the effect of catalyst design on the electrochemical performance is addressed.

2.2.1 Mechanism

Electrochemical CO_2 reduction follows the general cathodic reaction described below.[32]

$$xCO_2 + nH^+ + ne^- \longrightarrow \text{product} + yH_2O \tag{2.4}$$

The process of CO_2 reduction can be divided into several steps.[2]

1) Adsorption of CO_2 on the cathode surface
2) Proton-electron assisted activation of CO_2
3) Reaction pathway to the final product
4) Product desorption

This means the first key step for CO_2 reduction is the migration of CO_2 to the electrode interface. In an electrochemical cell with an aqueous electrolyte, this is achieved after the dissolution, equilibration, and bulk-to-interface transportation of CO_2 gas.[16,33] The dynamics of these steps heavily depend on the electrolyte composition and the resulting concentration gradients.[16,33] For a bicarbonate buffer electrolyte, the CO_2 hydration kinetics, as described in Equation 2.5, are slow, with $t_{1/2} = 19$ s.[16,23] As such, concentration gradients are especially relevant in this system.

$$CO_2(aq) + OH^- \longleftrightarrow HCO_3^- \tag{2.5}$$

Consequently, activation of the CO_2 molecule on the electrocatalyst surface occurs.[33] The exact activation mechanism is still debated within the field, but there is consensus that the proton-electron-assisted activation of CO_2 can lead to two different intermediates, as shown in Equations 2.6 and 2.7. These different intermediates will lead to dissimilar products, with *COOH being the most likely intermediate for CO formation and *OCHO for formic acid formation.[33,34]

$$* + CO_2 + H^+ + e^- \longrightarrow *OCHO \tag{2.6}$$

$$* + CO_2 + H^+ + e^- \longrightarrow *COOH \tag{2.7}$$

However, it is not clear yet if these activation reactions occur in a single step or two successive steps. In the latter case, the initial activation is only electron assisted, as shown in Equation 2.8. When this is followed by protonation, the same intermediates as in Equations 2.6 and 2.7 are obtained.[33,34]

$$* + CO_2 + e^- \longrightarrow *CO_2^- \tag{2.8}$$

Product	Half reaction	$E^0/[V_{RHE}]$
Carbon monoxide	$CO_2 + 2\,H^+ + 2\,e^- \longrightarrow CO + H_2O$	-0.10
Formic acid	$CO_2 + 2\,H^+ + 2\,e^- \longrightarrow HCOOH$	-0.12
Methane	$CO_2 + 8\,H^+ + 8\,e^- \longrightarrow CH_4 + 2\,H_2O$	0.17
Ethene	$2\,CO_2 + 12\,H^+ + 12\,e^- \longrightarrow C_2H_4 + 4\,H_2O$	0.08
Ethane	$2\,CO_2 + 14\,H^+ + 14\,e^- \longrightarrow C_2H_6 + 4\,H_2O$	0.14
Ethanol	$2\,CO_2 + 12\,H^+ + 12\,e^- \longrightarrow C_2H_5OH + 3\,H_2O$	0.09
Acetic acid	$2\,CO_2 + 8\,H^+ + 8\,e^- \longrightarrow CH_3COOH + 2\,H_2O$	0.11
Hydrogen Evolution Reaction	$2\,H^+ + 2\,e^- \longrightarrow H_2$	0
Oxygen Evolution Reaction	$2\,H_2O \longrightarrow O_2 + 4\,H^+ + 4\,e^-$	1.23

Table 2.1: CO_2 reduction products with their respective half-reaction and redox potential.[32]

Consequent electron- and/or proton-assisted steps complete the reaction pathway from the initial activation to the final product. For instance, the formation of carbon monoxide is described below.[33,35]

$$*COOH + H^+ + e^- \longrightarrow *CO + H_2O \tag{2.9}$$

$$*CO \longrightarrow CO + * \tag{2.10}$$

Many more reaction pathways are available and a broad range of products can be formed, including but not limited to C_2H_4, CH_4, and CH_3OH.[33,35,36] An overview of the most important products with their respective reactions and redox potentials is presented in Table 2.1. In addition, the competing Hydrogen Evolution Reaction (HER) is displayed. Notably, all of these reactions occur at similar potentials, which makes selectivity an important issue to address.[36]

2.2.2 Catalyst design

The catalyst design, especially the electrode composition and morphology, greatly affects the electrocatalytic performance. For product selectivity, the most crucial factor is the choice of catalyst material. The products and rate of CO_2 reduction depend on the binding strength of the intermediates to the catalyst, as described by volcano plots.[4,6–8] In 1993 Hori et al. classified metals by their dominant product. The group of CO-producing metals consisted of Au, Ag, and Zn. HCOOH was predominantly formed by Cd, In, Sn, Hg, Tl, and Pb. The only metal that could convert CO_2 in products beyond CO was Cu.[37]

The other important element for catalyst performance is electrode morphology. This includes crystal facet effects and size effects.[34] Experiments by Hoshi et al. in 1997 demonstrated that for Ag, the Ag(110) facet was most active for CO_2 reduction, followed by Ag(111) and Ag(100). These different performances arise from the different electronic configurations and structural parameters of the different facets.[10]

Multi-metallic catalysts offer modification of monometallic binding strengths, opening a huge field of potential catalysts for CO_2 reduction that has yet to be explored.[4,6,8] Both electronic and geometric effects are key factors for multi-metallic adsorption and reactivity properties.[6,8] Electronic effects are generally regarded as a result of the surface composition, whereas geometric effects are attributed to different atomic arrangements.[8] However, it should be realized that the atomic arrange-

ment contributes to the electronic structure of the catalyst.[4] Additionally, bifunctional mechanisms and ensemble effects can be observed in bimetallic catalysts.[21] To elaborate, bifunctional mechanisms involve two distinct active sites during catalysis that each fulfill their separate role, and ensemble effects can include blocking sites for undesirable side reactions or preventing the adsorption of inhibiting species.[21]

2.3 Synthesis of porous silver

The last part of the theoretical background focuses on the synthesis of porous Ag. There are several strategies for obtaining porous metals, such as dealloying an alloy, soft templating, and hard templating.[9,38] Using a template allows control over the pore morphology. In this work, a hard templating strategy is employed, where a 3D array of PMMA spheres forms the sacrificial template. As depicted in Figure 2.2, the electrodeposition of metal onto the template, and the consequent removal of the PMMA, results in a porous metal with the inverse structure of the spheres. Below, the formation of the template will be discussed, followed by an introduction to electrodeposition.

2.3.1 Template

Self-assembled colloidal crystals can be used as a hard template for periodic macroporous solids. They are formed by packing colloidal spheres into 3D arrays. In order to act as a template, the colloidal crystal should be easily removable, monodisperse (diameter variations <5-8%), and compatible with processing conditions.[39] Usually, silica, PS, or PMMA spheres are used for this.[39] Because of the subsequent electrodeposition step in the employed synthesis route, it is important that the template is fixed on a conductive substrate, and that it can withstand mechanical forces.

There are several strategies for achieving a 2D array of colloidal spheres, such as fluidic deposition with the Langmuir-Blodgett method, or spin-coating.[40] However, the assembly of an adhesive 3D array is rather challenging.

A method that is frequently used in literature for adhesive highly ordered 3D arrays, is an evaporation-induced assembly process.[23,41–43] This typically involves vertically immersing the substrate in a PS emulsion and slowly evaporating the liquid. The fluid flow to the meniscus drives the self-assembly of the colloidal spheres.[42] This method yields highly ordered colloidal crystals, and after further treatment highly ordered inverse opals. However, this strategy can take 4-5 days of constant heating, requires an excess of the colloidal suspension and has a limited layer thickness.[23]

A faster and more facile method for the self-assembly of spherical particles into a colloidal crystal is the droplet evaporation method. This is based on the drying of a droplet of suspended colloidal spheres, which means the self-assembly process

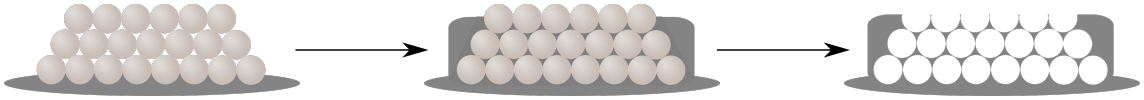

Figure 2.2: Schematic overview of hard templating strategy. First, a template is formed, then the metal is deposited onto the template, and lastly, the template is removed, resulting in a porous metal with the inverse structure of the template.

is a result of a combination of evaporation, surface tension, and capillary forces. However, the method often leads to non-uniform patterns because of the coffee stain effect, where most particles end up near the edge due to capillary flow.[40]

2.3.2 Electrodeposition

During electrodeposition or electrochemical deposition, solids are deposited under an electrochemical reduction reaction via

$$M^{x+} + xe^{-} \longrightarrow M(s). \tag{2.11}$$

The process takes place in an electrochemical cell (Figure 2.3) that consists of a cathode on which the deposit grows, an anode, an electrolyte solution, and a reference electrode, all connected to a power supply. Note that this setup is different from the H-type cell described in Section 2.1.1. Because electrochemical deposition is non-spontaneous, either a current (galvanostatic route) or potential (potentiostatic route) needs to be applied to drive the reaction. Using a potentiostatic technique is crucial when control of the deposit morphology is required, as explained in more detail below.[44]

Electrodeposition is a nucleation and growth process, which implies a critical energy is required for the nucleation of a specific morphology.[44] As a result, the deposit morphology depends on the applied potential, specifically on the nucleation overpotential, which is defined as the difference between the applied electrode potential and the nucleation potential. This relationship is highlighted in Figure 2.4, where the current is plotted as a function of the nucleation overpotential. At small nucleation overpotentials, the deposit growth is kinetically controlled, so the particle shape is determined by facet energies. However, moving to higher potentials the

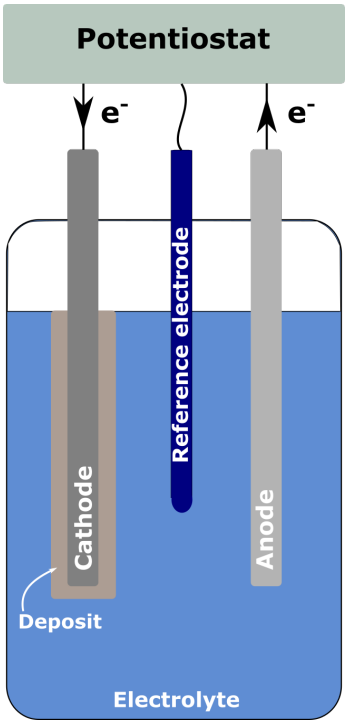

Figure 2.3: Schematic depiction of electrochemical deposition.

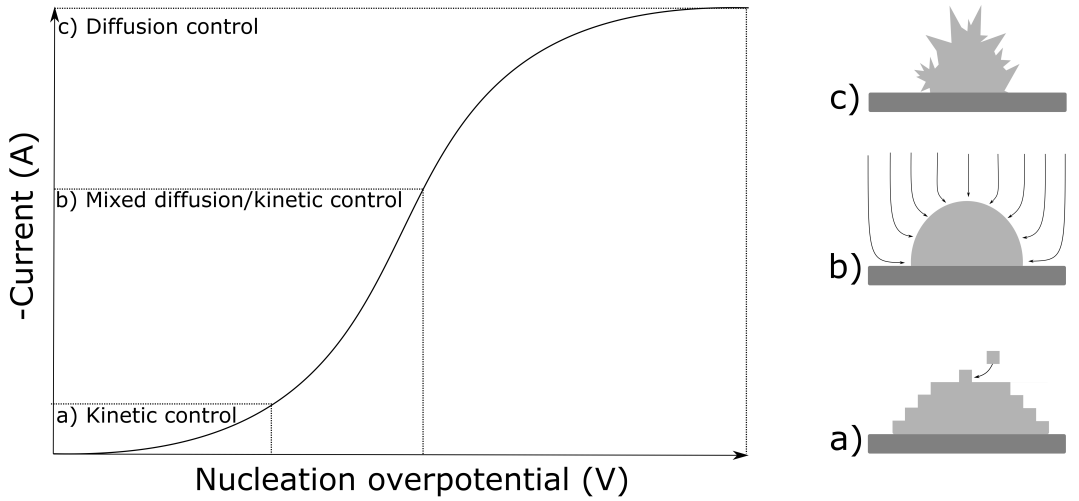

Figure 2.4: Plot of current against nucleation overpotential divided into 3 regimes. a) kinetic control, b) mixed diffusion/kinetic control, and c) diffusion control. Next to the graph, the corresponding island growth is depicted. a) Kinetically controlled island growth is dependent on facet energy. b) Mixed diffusion/kinetically controlled island growth often leads to hemispherical islands. c) Diffusion-controlled island growth can result in dendrite formation. Figure is adapted from Guo and Searson.[46]

growth is controlled by both diffusion and kinetics, which often results in hemispherical particles. At even higher potentials, diffusion controls the growth, and dendrite formation often occurs.[45,46]

Another important factor for morphology control is the electrolytic bath composition. In general, a salt is added to ensure a high conductivity of the bath, which is beneficial for the electrodeposit quality.[45] Also complexing agents can be introduced to the bath to control the deposit morphology, such as EDTA, HEDTA, NH_3, and thiourea.[18] For Ag, EDTA for instance leads to a more uniform coverage and when NH_3 is present in the solution, the deposition process shifts to the reaction below.[18,20]

$$Ag(NH_3)_2^+ + e^- \longrightarrow Ag + 2\,NH_3 \qquad E^0 = 0.373V\ vs\ NHE \qquad (2.12)$$

Chapter 3

Experimental

In this chapter, the experimental methodology will be described, starting with the materials. Then, the PMMA sphere template fabrication, the preparation of porous Ag, and the preparation of porous Ag-Cu are discussed. This is followed by a description of the morphological and electrochemical characterization, including the catalytic performance.

3.1 Materials

Sodium nitrate ($NaNO_3$, 99.0 %) and silver nitrate ($AgNO_3$, 99.9+%) were purchased at Thermo scientific. Ethylenediaminetetraacetic acid disodium salt dihydrate (EDTA, 98.5 to 101.5 %), copper (II) nitrate trihydrate ($Cu(NO_3)_2$, 99-104%), and Chelex®100 sodium form (50-100 mesh) were obtained from Sigma Aldrich. Silver foil (Ag foil, 0.025 mm thick, annealed, 99.95%) and Nafion D-520 dispersion (5% w/w in water and 1-propanol) were acquired from Alfa Aesar. Ammonia solution (NH_4OH, 28-30%, EMSURE®ACS) was purchased from Merck. Potassium bicarbonate ($KHCO_3$, 99.7%) was provided by Honeywell Fluka. Acetone (GPR RECTAPUR®) was acquired from VWR chemicals. All of these chemicals were used without further purification.

Ultrapure Millipore Milli-Q water was used for all experimental procedures. N117 nafion membranes were obtained from Ion Power and activated in ultrapure water of 100 °C for one hour. Glassy carbon disks (diameter 30 mm, thickness 2 mm, SIGRADUR®) were purchased from HTW. Separate glassy carbons were used for electrodeposition and electrocatalysis. Before every electrocatalysis, the glassy carbon was polished with diamond suspension (1, 0.25, and 0.05 µm, MetaDi) and microcloth from Buehler, followed by 5 minutes of sonication in ultrapure water. The electrochemical cell was cleaned in a 5% HNO_3 solution upon changing from Ag to Cu-containing catalysts. PMMA spheres were previously synthesized via surfactant-free emulsion polymerization at 70°C using 1.9 M methyl methacrylate.[47,48] The resulting batch contained 2.16 % w/w PMMA spheres in water with a diameter of 182 ± 22 nm.

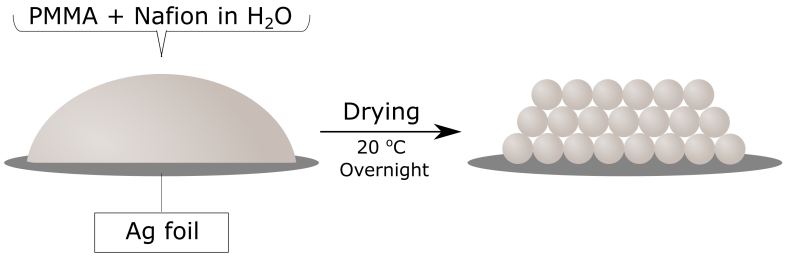

Figure 3.1: Schematic depiction of the droplet evaporation method. First, a suspension of PMMA spheres and Nafion in ultrapure water is put on an Ag foil substrate. A self-assembled PMMA sphere template is obtained after overnight drying at room temperature.

3.2 Template fabrication

The droplet evaporation method was utilized for the self-assembly of the PMMA spheres on Ag foil, as depicted in Figure 3.1. In a typical procedure, 20 mL of the 2.6 % w/w PMMA sphere suspension was mixed with 20 mL of ultrapure water and 300 µL Nafion®D-520 solution. Preliminary investigations demonstrated that this mixture resulted in the adhesion of the PMMA sphere template to the Ag foil substrate (further details in the supplementary information Section A.1). Subsequently, 2 mL of this mixture was applied to a 3 x 3 cm Ag foil substrate. The Ag foil was prepared via folding and unfolding to generate a mm-range surface roughness. Preliminary investigations had demonstrated that this was also a crucial factor for the adhesion of the PMMA sphere template to the Ag foil substrate, as shown in the supplementary information Section A.1. Finally, the templates were dried overnight at room temperature.

3.3 Preparation of porous Ag

Porous Ag was prepared by electrochemical deposition of Ag onto Ag foil in the voids of the self-assembled PMMA sphere template. The porous structure was generated by the subsequent removal of the PMMA sphere template, as presented in Figure 3.2. First, the standard synthesis of porous Ag will be described and this is followed by the variations applied to the procedure to change the Ag morphology.

For a typical synthesis, the Ag foil with the template was placed on top of a glassy carbon disc in a holder, together forming the working electrode with an exposed surface area of 3.8 cm^2. The holder was then immersed in an electrolyte solution and connected to the potentiostat (Autolab PGSTAT204), as illustrated in

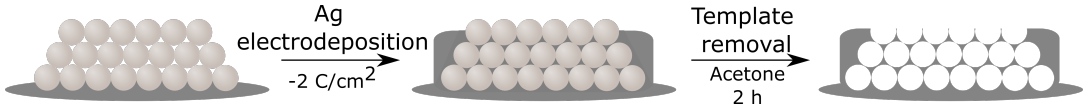

Figure 3.2: Schematic overview showing the preparation of porous Ag. Ag is electrochemically deposited on the PMMA sphere template with a charge cutoff of -2 C/cm^2 to achieve constant weight loading. Removing the template in acetone results in a porous Ag catalyst.

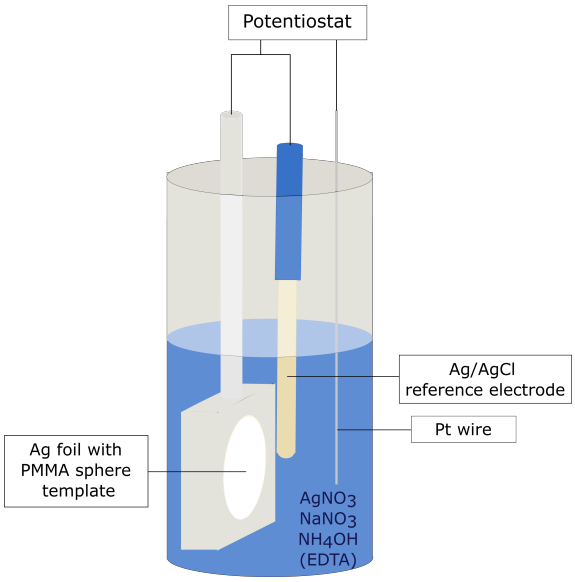

Figure 3.3: Schematic depiction of the electrochemical deposition setup. A holder containing Ag foil with a PMMA sphere template, a reference electrode, and a Pt wire are placed in an electrolytic bath containing 1 M $NaNO_3$, 0.05 M $AgNO_3$, 0.5 M NH_4OH, and 0.01 M EDTA.

Figure 3.3. This setup further contained a Pt wire as a counter electrode and an Ag/AgCl reference electrode, both connected to the potentiostat as well. A standard electrodeposition bath contained 1 M $NaNO_3$, 0.05 M $AgNO_3$, 0.5 M NH_4OH, and 0.01 M EDTA, based on the method by De Oliveira and Carlos.[49] A potential of - 0.1 V vs Ag/AgCl was typically applied to drive the electrodeposition. In order to achieve a constant weight loading, a charge cutoff of -2 C/cm^2 was employed. The syntheses were performed without agitation, as motivated in the supplementary information Section A.2. After electrodeposition, the samples were rinsed with ultrapure water and dried at room temperature. To dissolve the sacrificial template, the PMMA-containing samples were rinsed with acetone 3 times and subsequently immersed in 20 mL of acetone solution for 2 hours.

The electrodeposition conditions, applied potential and electrolyte composition, were varied to control the final morphology of the catalyst (supplementary information Section A.3). Here, one sample was prepared using an applied potential of -0.4 V vs Ag/AgCl and another sample explored the galvanostatic approach, using a constant current of -5 mA. In addition, samples were prepared without EDTA, half the amount of $NaNO_3$, or double the amount of NH_4OH. Note that the applied potentials for electrodeposition are not converted to the RHE scale because of the varying pH values of the electrolytic baths. An overview of the used parameters can be found in Table 3.2. Every synthesis was done in triplicate to enable sample characterization, and with and without the PMMA sphere template.

Table 3.1: Experimental conditions used for porous and non-porous Ag samples.

Name	$AgNO_3$ (M)	$NaNO_3$ (M)	EDTA (M)	NH_4OH (M)	Potential ($V_{Ag/AgCl}$)
Standard	0.05	1.0	0.01	0.5	-0.1
- 0.4 V	0.05	1.0	0.01	0.5	-0.4
-5 mA	0.05	1.0	0.01	0.5	Variable[1]
0.5 M $NaNO_3$	0.05	0.5	0.01	0.5	-0.1
0 M EDTA	0.05	1.0	0	0.5	-0.1
1 M NH_4OH	0.05	1.0	0.01	1	-0.1

1. The current was kept constant at -5 mA. Employing a galvanostatic method results in a variable potential.

3.4 Exploratory research: preparation of porous Ag-Cu

In order to explore the full potential of the template-based synthesis, bimetallic Ag-Cu catalysts were prepared. Preliminary research described in the supplementary information Section A.4 demonstrates that a porous Ag-Cu alloy prepared by co-deposition is not feasible. Therefore, the aim was to deposit a small amount of copper on porous silver. For this, in addition to a standard Ag bath, a Cu-containing electrodeposition bath was prepared. This bath consisted of 0.1 M $Cu(NO_3)_2$, 1 M $NaNO_3$, 0.01 M EDTA and 0.6125 M NH_4OH. The NH_4OH concentration was higher than for the Ag bath because preliminary research demonstrated that a lower amount of NH_4OH resulted in undesirable blue $Cu(OH)_2$ precipitation, as shown in the supplementary information Section A.4.

First, Ag was deposited on Ag foil with PMMA spheres at a potential of -0.2 V vs Ag/AgCl with a charge cutoff of - 7.6 C. Then, the electrode was rinsed with ultrapure water, and placed in the Cu-containing bath. Cu was deposited at a potential of -0.5 V vs Ag/AgCl with a charge cutoff of - 0.5 C. A reference sample was prepared by electrodeposition of Cu onto Ag foil with the PMMA sphere template. This electrode was only placed in the Cu bath, and a potential of -0.5 V vs Ag/AgCl was applied until a charge cutoff of -2 C/cm^2. An overview of the electrodeposition conditions used for these Cu-containing samples and Standard Ag as a reference sample can be found in Table 3.2. Note that the reduction of Cu^{2+} to Cu involves 2 electron transfers, whereas the reduction of Ag^+ to Ag involves 1, so the deposited weight is not equal when similar charge cutoff values are used. The PMMA sphere template was removed using the standard removal procedure of 2 hours of dissolution in 20 mL of acetone before drying overnight.

Table 3.2: Overview of experimental conditions used for Cu-containing samples, and standard porous Ag as a reference. The Ag bath contains 1 M $NaNO_3$, 0.05 M $AgNO_3$, 0.5 M NH_4OH, and 0.01 M EDTA, and the Cu bath contains 0.1 M $Cu(NO_3)_2$, 1 M $NaNO_3$, 0.01 M EDTA and 0.6125 M NH_4OH

	Ag bath		Cu bath	
Name	Potential ($V_{Ag/AgCl}$)	Charge (C/cm^2)	Potential ($V_{Ag/AgCl}$)	Charge (C/cm^2)
Cu	-	-	-0.5	-2
Ag-Cu	-0.2	-2	-0.5	-0.13
Standard Ag	-0.1	-2	-	-

3.5 Morphological characterization

All electrocatalysts were characterized using high-resolution scanning electron microscopy (HR-SEM), in order to determine the morphology and pore structure. These measurements were conducted on FEI Helios G3 Nanolab operated with an acceleration voltage of 5.00 kV and an electron beam current of 0.2 nA. Sample preparation involved attaching a small piece of the electrode to the sample holder with carbon tape. On the Ag-Cu sample, energy dispersive X-ray spectroscopy (EDX) with an acceleration voltage of 15 kV was performed as well to determine the catalyst composition.

The pore size diameter was determined by manual analysis of HR-SEM micrographs with ImageJ software. A total of 200 different pores were measured in 3 different places on the standard sample. In addition, double layer capacitance measurements were performed to determine the electrochemical surface area. This is further described in the supplementary information Section A.5.

Preliminary investigations showed that the characterization of the surface area and pore volume by nitrogen physisorption was unviable. In addition, it was not possible to separate the peak contributions of deposited Ag from Ag foil in X-ray diffractograms.

3.6 Electrochemical characterization

Several electrochemical measurements were performed on each electrode in an H-type cell, such as cyclic voltammetry (CV), double layer capacitance (DLC), and chronoamperometry (CA). Figure 3.4 shows the electrochemical cell that was used for these measurements. As can be seen in this image, the anodic and cathodic compartments, each with a volume of 18 mL, were separated by an activated Nafion®proton exchange membrane. Both sides were filled with 15 mL of a 0.1 M $KHCO_3$ solution. The prepared electrodes were placed on top of a glassy carbon disk and positioned on the cathodic side as the working electrode. The exposed geometric surface area of the Ag electrodes was 3.8 cm^2. This compartment also contained an Ag/AgCl reference electrode and a magnetic stirring bean and was connected to the gas chromatograph (GC). A Pt disk was employed as a counter electrode on the anodic side. CO_2 gas and Ar gas were flowed through the cathodic and anodic compartments, respectively, at a flow rate of 10 mL/min. To convert the measured potential vs Ag/AgCl to the potential vs RHE, Equation 3.1 was used.

$$E_{RHE} = E_{Ag/AgCl} + E^0_{Ag/AgCl} + 0.059pH. \tag{3.1}$$

Here, $E_{\mathrm{Ag/AgCl}}$ is the measured potential vs Ag/AgCl and $E^0{}_{\mathrm{Ag/AgCl}}$=0.198 V.[50] The pH of a CO_2 saturated 0.1 M $KHCO_3$ solution is 6.8. However, it is important to realize that the local pH of the catholyte at the catalyst might differ from the bulk pH and that that can cause deviations on the RHE scale. This is especially relevant in porous systems which exhibit mass transport limitations.[34]

3.6.1 Cyclic voltammetry

To determine the onset potential, a CV was recorded between 0.1 V and -1.4 V vs RHE with a scan rate of 0.01 V/s for 5 cycles, without agitation. For quantification

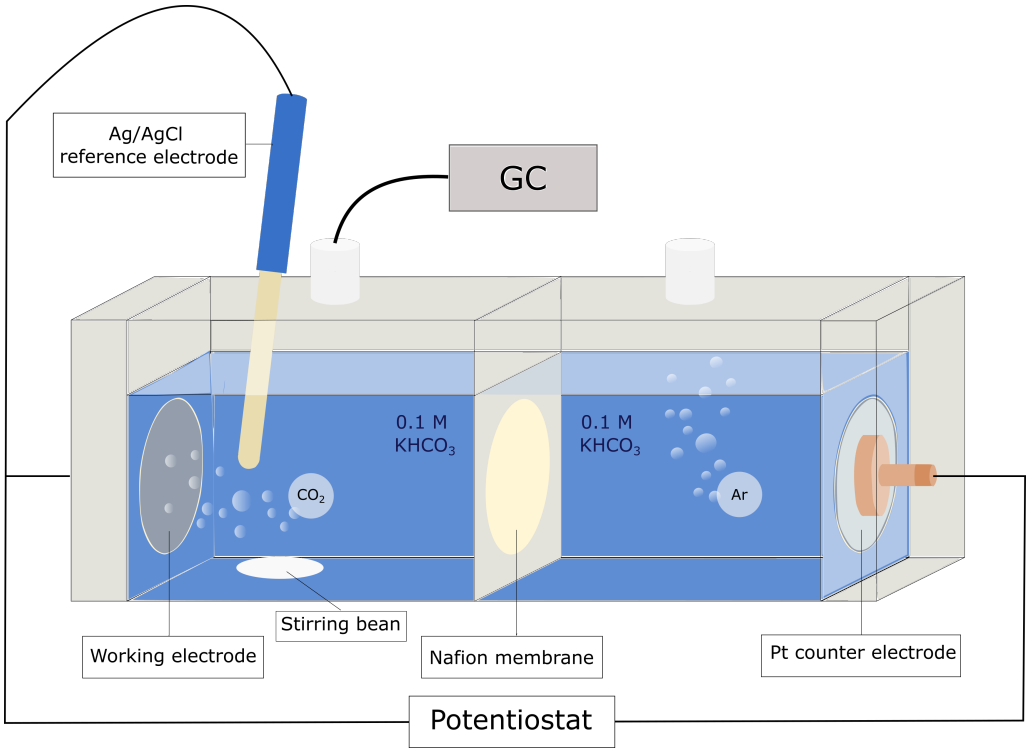

Figure 3.4: H-type electrochemical cell used for electrochemical measurements. CO_2 gas flows through the cathodic compartment (left), which contains the working electrode, an Ag/AgCl reference electrode, and a stirring bean and is directly connected to the GC. A Pt counter electrode is placed on the anodic side (right). Both compartments contain a 0.1 M $KHCO_3$ solution as electrolyte.

of the onset potential, a threshold value of -0.3 mA for the 5th cycle was used. In addition, this operation reduces the silver oxide layer.

3.6.2 Double layer capacitance

DLC was performed on each sample without agitation to determine the electrochemical surface area (ECSA). For the samples Standard, -0.4 V, and -5 mA a potential window of 0.6 - 0.4 V vs RHE and scan rates of 0.005, 0.01, 0.02, 0.04, and 0.08 V/s were used. All other samples used 0.005, 0.01, 0.02, 0.04, 0.08, 0.1, 0.2, 0.3, 0.4, 0.5, 0.6, 0.7, 0.8, 0.9, and 1.0 V/s as scan rates. The samples 0.5 M $NaNO_3$, 0 M EDTA, and 1 M NH_4OH were scanned in a potential window of 0.6 - 0.2 V vs RHE, whereas Cu and AgCu needed a slightly shifted potential window of 0.55 - 0.2 V to remain in the non-faradaic region. An overview of all of these employed parameters per sample can be found in Table 3.3. Each scan rate was cycled 5 times before moving on to the next one.

3.6.3 Catalytic performance

For a catalytic test, the catholyte was stirred at 400 rpm and saturated with CO_2 (10 mL/min) for a minimum time of an hour. Consequent chronoamperometry (CA) measurements were conducted at potentials of -0.7, -0.9, -1.2, and -1.4 V vs RHE for 1890 s per potential. This cycle was conducted three times in order to investigate

Table 3.3: An overview of the DLC parameters per sample.

Name	Scan rate (V/s)	Potential (V_{RHE})
Standard	0.005 - 0.08[1]	0.6 - 0.4
- 0.4 V	0.005 - 0.08[1]	0.6 - 0.4
-5 mA	0.005 - 0.08[1]	0.6 - 0.4
0.5 M $NaNO_3$	0.005 - 1.0[2]	0.6 - 0.2
0 M EDTA	0.005 - 1.0[2]	0.6 - 0.2
1 M NH_4OH	0.005 - 1.0[2]	0.6 - 0.2
Cu	0.005 - 1.0[2]	0.55 - 0.2
Ag-Cu	0.005 - 1.0[2]	0.55 - 0.2

1. 0.005, 0.01, 0.02, 0.04 and 0.08 V/s
2. 0.005, 0.01, 0.02, 0.04, 0.08, 0.1, 0.2, 0.3, 0.4, 0.5, 0.6, 0.7, 0.8, 0.9, and 1.0 V/s

the stability. During CA measurements, gaseous products were monitored by the on-line GC (CompactGC$^{4.0}$, Global analyser solutions). At each potential 10 gas samples were analyzed using a thermal conductivity detector for H_2 and a flame ionization detector for CO, CH_4, C_2H_4, and C_2H_6. As Cu-containing samples could also form liquid products, 1 mL of catholyte was extracted after every potential and replenished by 1 mL of 0.1 M $KHCO_3$ solution. These samples were analyzed with nuclear magnetic resonance spectroscopy (NMR). NMR samples were prepared by mixing 500 µL of the catholyte with 100 µL of a solution containing 10 mM DMSO and 50 mM phenol as internal standards. The ^{1}H NMR measurements were performed on a 400 MHz Varian VNMRS spectrometer. Post-catalysis, the electrodes were rinsed with ultrapure water and studied with HR-SEM.

3.6.4 Catalyst stability

As a means to understand the post-reaction morphology, catalysis on the 0.5 M $NaNO_3$ sample was performed where the catalyst morphology was studied at different steps. A setup similar to the one used for electrodeposition, shown in Figure 3.3, was employed. However, in this case, the electrode was immersed in CO_2-saturated 0.1 M $KHCO_3$. Note that there was no CO_2 flow in this system. First, 5 CV cycles between 0.1 and -1.4 V vs RHE were measured with a scanning rate of 0.01 V/s. After this step, a sample from the silver electrode was taken, which resulted in a reduction in the electrode size. The remaining electrode was put back into the holder. Then, potentials of -0.7, -0.9, -1.2, and -1.4 V vs RHE were each applied for 1890 s. After every potential, another SEM sample was taken, and the electrolyte solution was exchanged for new CO_2-saturated 0.1 M $KHCO_3$. All of the samples were analyzed with HR-SEM.

Chapter 4

Results and discussion

In this chapter, the results will be presented, starting with a discussion of porous Ag, followed by exploratory research on porous Ag-Cu.

4.1 Porous Ag

Porous Ag was prepared by Ag electrodeposition on a PMMA template on Ag foil. To obtain 6 different Ag morphologies, either the standard applied potential or the concentration of one of the complexing agents was modified, see Section 3.3. Note that the sample name corresponds to the varied parameter, with potentials reported against Ag/AgCl. To understand how these reaction parameters influence the catalyst morphology and hence the catalyst performance, the morphology of the different Ag samples will be discussed first. Then, these morphologies will be related to the electrocatalytic performance.

4.1.1 Morphology

To determine the morphology of the porous Ag catalysts, high-resolution scanning electron microscopy (HR-SEM) images were taken. Figure 4.1 shows the HR-SEM images of the porous catalysts. From this figure, it is clear that all samples, made under all electrodeposition conditions, display porosity in accordance with the inverse of the PMMA sphere template. Here, a slightly disordered pore structure is found, unlike the inverse opal Ag structure obtained by Yoon et al.[23] This is attributed to the addition of Nafion solution to the PMMA suspension, which prevented a close packing of the PMMA spheres, as discussed in the supplementary information Section A.1. The average pore size of the Standard sample was determined to be 183 $\pm$ 28 nm. This is very similar to the PMMA sphere size of 182 $\pm$ 22 nm. Both of their size distributions are presented in the supplementary information Section A.6.

Interestingly, the SEM micrographs demonstrate that upon changing the electrodeposition conditions, the Ag morphology around the template varies accordingly. Specifically, -0.4 V and 0 M EDTA show coral-like structures, resulting in hierarchical porosity. This is caused by the formation of dendritic structures as a result of applying a potential in the diffusion-controlled regime and the absence of the dendrite formation inhibiting EDTA, respectively.[20,45] All the other porous samples have a flat structure. However, even on a nanoscale, differences between the porous samples are evident. Figure 4.2 provides zoomed-in HR-SEM images of porous Ag

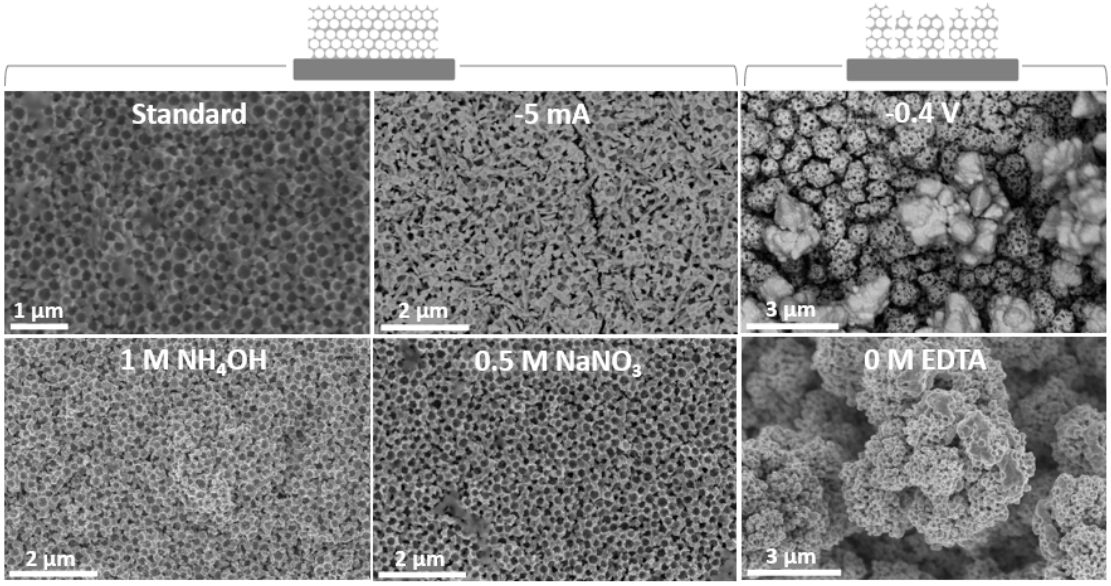

Figure 4.1: HR-SEM images of porous catalysts. Standard, -5 mA, 1 M NH_4OH, and 0.5 M $NaNO_3$ show a flat structure around the porosity, while -0.4 V and 0 M EDTA have a coral-like structure, resulting in additional macropores.

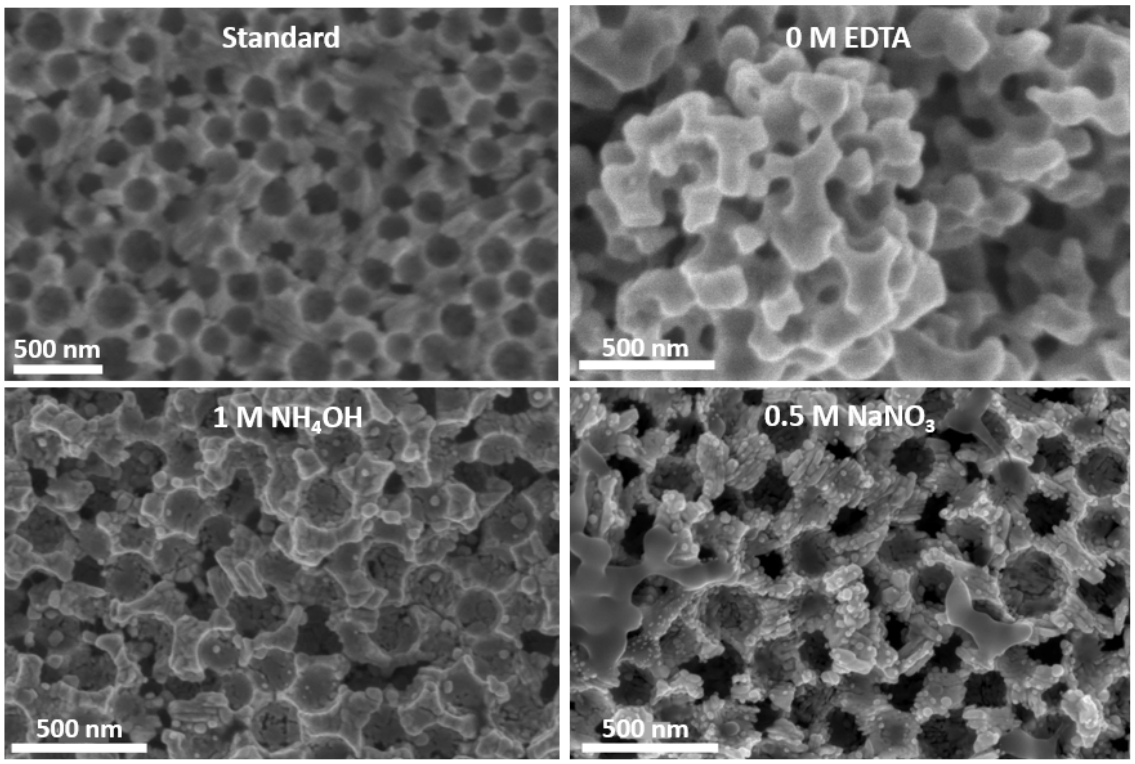

Figure 4.2: Zoomed in HR-SEM images of porous Ag. Standard and 0 M EDTA have a smooth Ag morphology around the pores, whereas 1 M NH_4OH and 0.5 M $NaNO_3$ contain and consist of nanoparticles, respectively.

samples Standard, 0 M EDTA, 1 M NH_4OH, and 0.5 M $NaNO_3$. In contrast to the Standard sample, the morphology around the pores shows some roughness for 1 M NH_4OH and consists of nanoparticles for 0.5 M $NaNO_3$. This might indicate that an increased NH_4OH concentration of 1 M or a decreased $NaNO_3$ of 0.5 M results in a less homogeneous deposit morphology. However, the resolution of the SEM images of Standard and 0 M EDTA is lower than for 1 M NH_4OH, and 0.5 M $NaNO_3$, which might have affected the observations.

In order to determine the effect of the PMMA sphere template on the Ag deposit morphology, the SEM images of porous and non-porous Ag prepared with the same electrodeposition parameters are compared. When relating the structure of the porous catalysts to the structure of their non-porous equivalents, as done for the Standard, -0.4 V and -5 mA samples in Figure 4.3, it can be observed that the morphology around the porosity corresponds to the morphology of the non-porous counterpart. The HR-SEM images of 0 M EDTA and 1 M NH_4OH are included in the supplementary information Section A.7. The needle-like lines that can be found between pores in the Standard sample are the main characteristic of its non-porous counterpart as well. Similarly, a dendritic structure is recognizable in both porous and non-porous -0.4 V, and filament structures can be seen in both -5 mA samples. It appears that the template does not inhibit the nucleation process for obtaining a specific morphology, which to the best of our knowledge has not been demonstrated yet in literature. This implies that a PMMA sphere template can be used to introduce porosity in any previously defined Ag morphology.

Double layer capacitance measurements were used to determine the electrochemical surface area (ECSA) of the catalysts. More details on how the ECSA was subtracted from these measurements are described in the supplementary information Section A.5. Data obtained at scan rates higher than 0.08 V/s was discarded for this analysis to ensure a fair comparison between the catalysts. In addition, the scan rate of 0.005 V/s was neglected because it was found that competing faradaic processes contributed significantly to the measured current at this rate.[29]

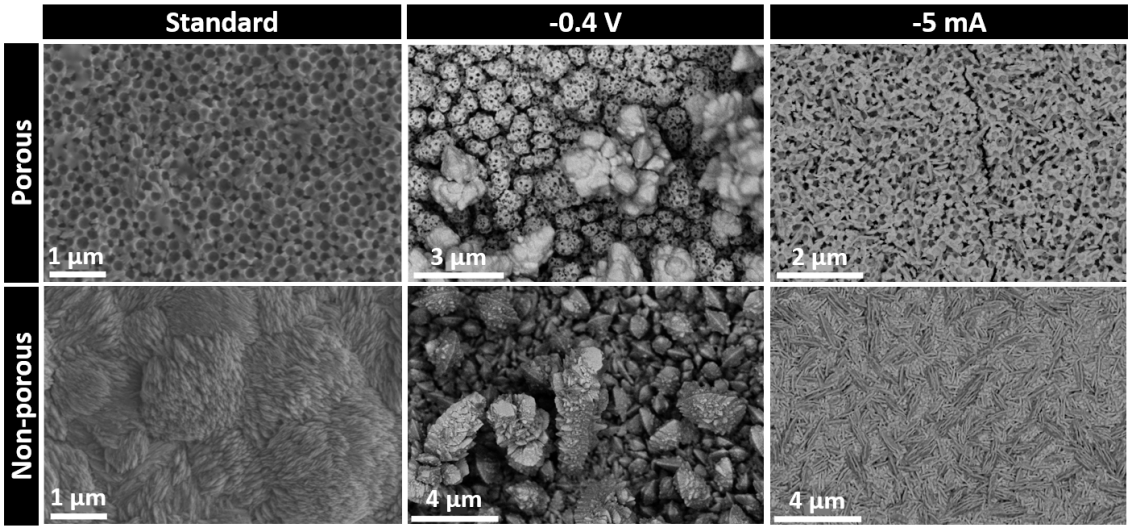

Figure 4.3: Comparison of HR-SEM images of porous Ag and the non-porous equivalent. The porous and non-porous Standard samples both show needle-like lines. Both -0.4 V samples have a dendritic structure, and filaments can be seen in both -5 mA samples.

The factor F by which the surface area increased as a result of porosity, was calculated by

$$F = \frac{ECSA_{\text{porous}}}{ECSA_{\text{non-porous}}}. \tag{4.1}$$

Table 4.1 shows the obtained ECSA and F values of all catalysts. The ECSA of all porous samples are relatively close to each other - compared to non-porous samples - with the exception of 0.5 M $NaNO_3$ having a significantly higher value (291.3 cm^2 versus 115.6 - 161.8 cm^2). This exception might be an effect of the additional surface roughness caused by the high amount of nanoparticles observed in Figure 4.2. Another possibility is that an error occurred during the measurement or analysis (supplementary information Section A.5 Table A.2). For this reason, it would be recommended to implement lead underpotential deposition as an additional technique for the determination of the ECSA. The ECSA of all non-porous samples showed a relatively larger variation since the dendritic samples (-0.4 V and 0 M EDTA) had a higher ECSA than the flat samples as a result of their macroporosity (18.5 - 169.4 cm^2). In addition, non-porous -0.4 V shows additional surface roughness from a nano-sized spike morphology (Figure 4.3). As the large variations in ECSA for non-porous Ag resulting from morphological differences are not as extensive for porous Ag, it follows that ECSA is dominated by the porosity in porous Ag. For all but -0.4 V, the surface area was increased after introducing porosity. Specifically, the ECSA of all flat structures (Standard, -5 mA, and 1 M NH_4OH) increased with consistent F values of roughly 6.6. These results contribute to a better understanding of the effect of porosity on the electrochemical surface area of the catalyst.

Table 4.1: ECSA and F determined with DLC for porous and non-porous catalysts.

Name	$\text{ECSA}_{\text{porous}}$ (cm^2)	$\text{ECSA}_{\text{non-porous}}$($cm^2$)	F ($=\frac{ECSA_{\text{porous}}}{ECSA_{\text{non-porous}}}$)
Standard	122.2	18.5	6.62
- 0.4 V	161.8	169.4	0.955
-5 mA	154.4	23.58	6.55
0.5 M $NaNO_3$	291.3	-	-
0 M EDTA	115.6	51.05	2.26
1 M NH_4OH	136.1	20.85	6.52

In order to understand if these results match the expected effect of using a spherical template on the catalyst surface area, a numerical model has been developed. Equation 4.2 describes F as a function of the number of layers n, for $n \leq n_{\max}$.

$$F = (0.5 + \sum_{k=1}^{n-1} ab^{n-1})\pi \tag{4.2}$$

Here, a is a correction factor for the loss of surface area when 2 spheres are in contact. An a value of 0.8 corresponds to each sphere losing 10% of its surface area as a result of the formed gap. The factor b corrects for the inaccessibility of pores resulting from silver growing around an entire sphere, as can be seen in the HR-SEM images in Figure 4.2. If 70% of the spheres in layer 1 are in contact with layer 2, b would be 0.7. A complete derivation of this equation and the underlying assumptions can be found in the supplementary information Section A.8. Interestingly, this equation does not

directly depend on the sphere size. However, n_{max} increases when the particle size decreases (assuming a constant Ag layer thickness), so a higher F can be reached by smaller spheres. This happens if the number of layers at which F plateaus as a result of b is higher than n_{max} of the larger spheres. In other words, using smaller spheres will lead to a higher surface area if sufficient pore connectivity is achieved.

It is important to note that a and b are estimated based on SEM data. The results of this model can therefore contain a high error. In addition, this model can not be applied to catalysts with a hierarchical pore system.

Based on the HR-SEM images, a and b were both estimated to be 0.7 for the Standard, -5 mA, and 1 M NH_4OH samples. Figure 4.4 shows the model with the selected values for a and b, as well as the measured values for F. It is clear that the value of F obtained by the model (6.7) shows a high similarity to the measured values of F (6.62, 6.55, and 6.52 for Standard, -5 mA and 1 M NH_4OH, respectively). Note that for the Ag catalysts, the number of layers is very roughly estimated from a SEM image presented in the supplementary information Section A.8 Figure A.22, but as the F stabilizes after $n = 10$, it is not expected to affect the interpretation. This also suggests that for porous structures with poor pore connectivity, there is no added value in having more than a certain amount of layers (e.g. 10 in the case of $a = 0.7$ and $b = 0.7$). In order to further validate the model, data on the inverse opal Ag (Ag-IO) catalyst of Yoon et al. was used as well.[23] Their results gave a value of $F = 20$ for $n = 18$ layers. To simulate their system, values of a and b of respectively 0.3 and 1.0 were selected based on their SEM images. Again, the model reaches a similar value of $F = 17.6$ at 18 layers, demonstrating this simple model is able to approximate the surface area increase generated by spherical templating.

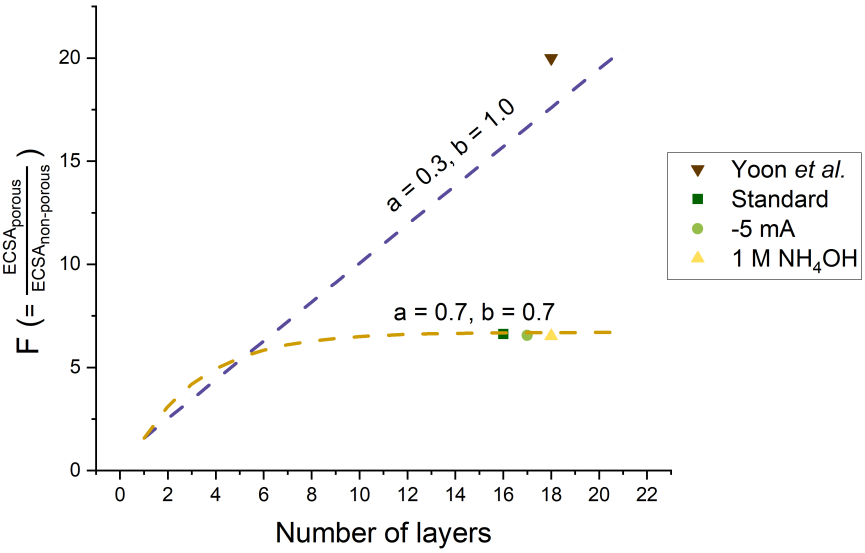

Figure 4.4: Simulation (dashed) of F (factor by which the surface area increased as a result of porosity) with $a = 0.7$ and $b = 0.7$ for Standard, -5 mA, and 1 M NH_4OH, and a = 0.3 and b = 1.0 for Ag-IO of Yoon et al..[23] Symbols represent the values obtained from DLC measurements. Note that the number of layers for samples Standard, -5 mA, and 1 M NH_4OH are very rough estimations.

4.1.2 Electrochemical performance

Knowing the differences in morphology, it is interesting to determine how this affects the catalytic performance. Therefore, in this section, the selectivity, activity, and stability of porous Ag catalysts are discussed. Gas products with a FE lower than 2% at -1.4 V vs RHE have been neglected. Note that the data is not corrected for uncompensated resistance and that the measured potential vs Ag/AgCl is converted to the potential vs RHE via Equation 3.1 in Section 3.6.

4.1.2.1 Selectivity

In this first section, the effect of porosity and morphology on the catalyst selectivity will be discussed. For electrocatalysis, the faradaic efficiency (FE) is generally used as a descriptor of selectivity. Figure 4.5 provides both FE_{CO} and FE_{H2} as calculated via Equation 2.3 in Section 2.1.3. What immediately stands out is that the FE_{CO} values of porous samples are generally higher than the FE_{CO} values of the non-porous samples. The opposite trend is noticeable for FE_{H2}, where the highest values are obtained by non-porous samples. In other words, it seems like introducing porosity enhances the CO selectivity, while suppressing the H_2 selectivity.

These effects are the most extreme at the least negative potential (-0.7 V vs RHE). Here, the CO FE is for example increased from 21 to 60 %, while the H_2 FE is suppressed from 46 to 21 % by introducing porosity in the Standard sample. On the other hand, at the most cathodic potential (-1.4 V vs RHE), the FE_{CO} rises only from 70 to 74 % and the FE_{H2} drops from 16 to 8 % as a result of the porous structure.

Remarkably, not for all of the samples marked differences between porous and non-porous Ag can be observed. Specifically, the non-porous samples with a coral-like structure (-0.4 V and 0 M EDTA) have comparable CO and H_2 selectivity as their porous equivalents. What is even more surprising, is that the non-porous -0.4 V sample has a higher FE_{CO} and a lower FE_{H2} than the porous sample at every potential. For the 0 M EDTA sample, it depends on the potential whether the porous or the non-porous Ag has the highest selectivity. Previously, in a study of porous Ag by Yoon et al., only significantly improved CO selectivities have been reported.[23] However, the findings of this work imply that this trend generally observed in litera-

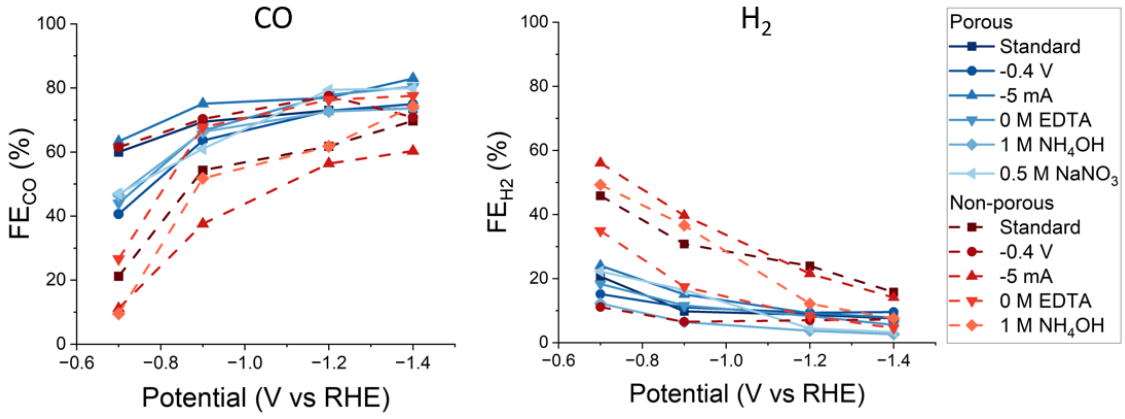

Figure 4.5: CO and H_2 faradaic efficiencies of all porous (blue) and non-porous (red, dashed) samples. The symbols indicate the synthesis conditions.

ture can be inverted or absent for certain Ag morphologies. Seemingly, the potential of introducing porosity to tune the catalyst selectivity depends on the non-porous Ag morphology. A possible explanation of these results would involve the catalyst surface area and mass transport conditions of the structures, which will both be discussed in more detail in the following section.

4.1.2.2 Activity

The previous section has focused on the effect of introducing porosity to Ag catalysts on the CO selectivity and demonstrated that this is affected by the Ag morphology. In order to further understand the effects of porosity on different Ag morphologies, the catalytic activity will now be discussed in terms of the onset potential, and the CO and the H_2 partial current density.

The onset potential can be extracted from cyclic voltammetry (CV) measurements. Figure 4.6 provides the current vs potential plot of the CV measurement from the Standard porous and non-porous sample, measured between 0.1 and -1.4 V vs RHE with a scan rate of 0.01 V/s. Before proceeding to examine the onset potential, it should be highlighted that in the first cycle, the current reaches higher values between 0.1 and -0.6 V vs RHE than for other cycles, with a peak around -0.1 V vs RHE. This is a result of the reduction of the oxidized silver layer. For determination of the onset potential, the first cycle is therefore not considered.

Turning back to Figure 4.6, it can qualitatively be observed that the porous sample reaches currents with a larger magnitude at less cathodic potentials, implying a lower onset potential for the porous catalyst. This is confirmed by employing a definition of the onset potential as the potential where the current reaches a predefined threshold value of -0.3 mA. Under these circumstances, the onset potential

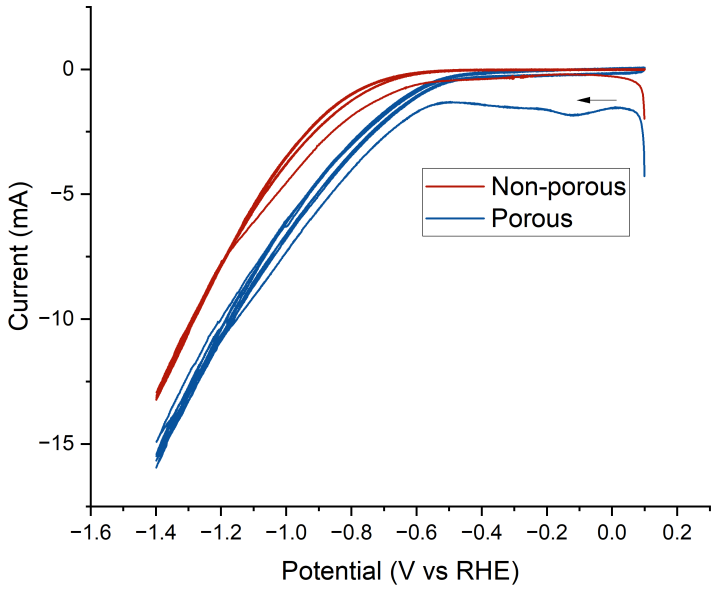

Figure 4.6: Current vs potential plot of CV measurement of porous (blue) and non-porous (red) Standard sample between 0.1 and -1.4 V vs RHE obtained with a scan rate of 0.01 V/s. The arrow indicates the beginning and scanning direction.

of the porous and non-porous samples are -0.41 and -0.65 V vs RHE, respectively, meaning the onset potential has shifted to a less cathodic potential by 0.24 V after introducing porosity. The same trend was observed for all other Ag catalysts, except for -0.4 V, which is the only condition where non-porous Ag has a higher surface area than porous Ag. This demonstrates that most likely, the higher surface area of porous catalysts causes the onset potential to shift to a less negative value. Interestingly, a shift in the onset potential of 0.15 V was found by Wang et al. when they compared porous Ag foams to Ag foil.[15] It is not reported how their onset potential was defined, but the qualitative trend is in line with the findings of this work. They reasoned that the shift was a result of the higher surface area of the porous catalyst. In literature, it is also demonstrated that the onset potential is inherently dependent on the catalyst surface area.[31]

While the observed shifts in onset potential of this study can mostly be attributed to increased ECSA, there might be more contributing factors. At -0.41 vs RHE, the current of porous Ag is -0.3 mA, whereas the current of non-porous Ag reaches 0.03 mA. The 10-fold increase of the current can not be entirely ascribed to the factor 6.62 increase in the ECSA. Other contributing factors could be local pH effects caused by poor mass transport capabilities in the porous structure or a specific catalysis-enhancing characteristic of the pore morphology.

The partial current density (j_{product}) corresponds to the activity of the catalyst towards a specific product and is calculated by multiplying the faradaic efficiency (FE) with the total current density (j_{tot}). Here, j_{tot} is normalized by the geometric surface area of the catalysts. The j_{CO} values of all porous and non-porous samples versus the applied potential are presented in Figure 4.7. It is evident that the porous Ag catalysts generally produce more CO compared to their non-porous counterparts, which is likely a result of their higher surface area. For example, at -1.4 V vs RHE, j_{CO} reaches values between 3.45 and 4.25 mA/cm^2 for porous samples, while the range for non-porous catalysts is between 2.21 and 2.97 mA/cm^2.

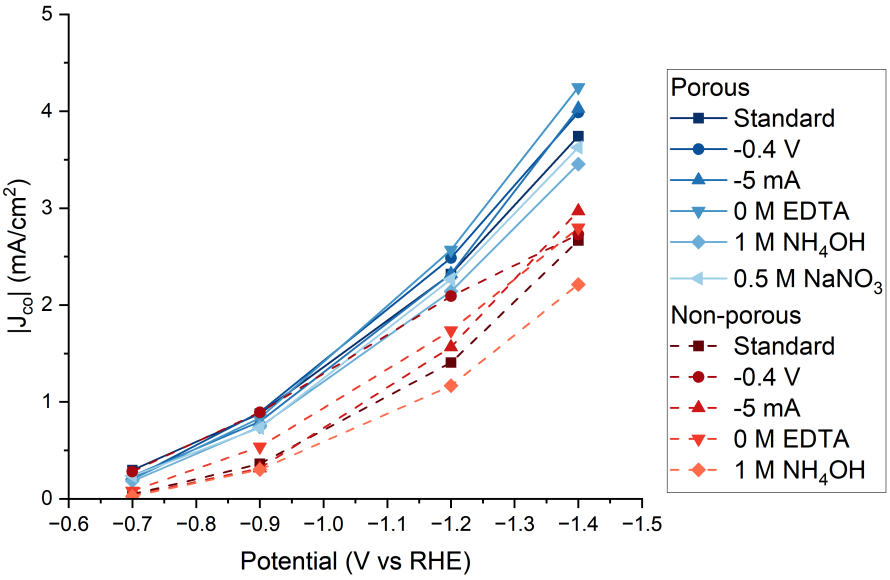

Figure 4.7: CO partial current densities of all porous (blue) and non-porous (red, dashed) samples. The symbols indicate the synthesis conditions.

When plotting the j_{CO} values against the ECSA of the catalysts as done in Figure 4.8, it becomes clear that the activity is directly proportional to the surface area at -0.7 V. Note that this entails that the non-porous -0.4 V sample outperforms the porous -0.4 V sample as it also has a higher surface area and that the 0.5 M $NaNO_3$ sample is an outlier, as discussed previously in Section 4.1.1. Interestingly, the ratio R between the porous and non-porous j_{CO}, as described by Equation 4.3, also corresponds to F, the ratio between the porous and non-porous ECSA (Equation 4.1).

$$R = \frac{j_{\text{CO, porous}}}{j_{\text{CO, non-porous}}} \tag{4.3}$$

To illustrate, (R, F) is (6.3, 6.6), (0.76, 0.96), (6.9, 6.6), (2.5, 2.3), and (7.0, 6.5) for the Standard, -0.4 V, -5 mA, 0 M EDTA, and 1 M NH_4OH samples, respectively. These findings highlight that the enhancement in CO_2 conversion of porous structures is predominantly an effect of their larger surface area.

It has been suggested by Yoon et al. that on top of the surface area effect found for both porous Ag and Au, mesostructure-induced transport limitations contribute to a higher j_{CO} in porous Ag.[23,51] They found that the intrinsic CO activity of Ag-IO increased by a factor of 3 at -0.8 V vs RHE ($R = 3F$).[23] However, this does not appear to be the case for the porous Ag samples presented here ($R = F$). A possible explanation for this difference is that the pore structure in the Ag samples from Yoon et al. demonstrates a higher level of order and better pore connectivity.

On the other hand, the results of this work are in agreement with the study of Park et al. They prepared Cl-modified nanoporous Ag nanowires and found that they achieve a j_{CO} that is 20 times as high as j_{CO} of Ag foil at -0.8 V vs RHE.[52] If the Standard porous Ag sample is compared to Ag foil, j_{CO} increases by a factor of 16 at -0.7 V vs RHE (supplementary information Section A.9).

To determine the effect of the morphology surrounding the pores, the subtle differences in j_{CO} between porous Ag samples are important. It was assumed that at -0.7 V these differences are smaller than the error of the measurement. Hence, further analysis of the activity towards CO presented in Figure 4.7 was conducted at -1.4 V vs RHE, where the distance between j_{CO} values of porous samples is more substantial.

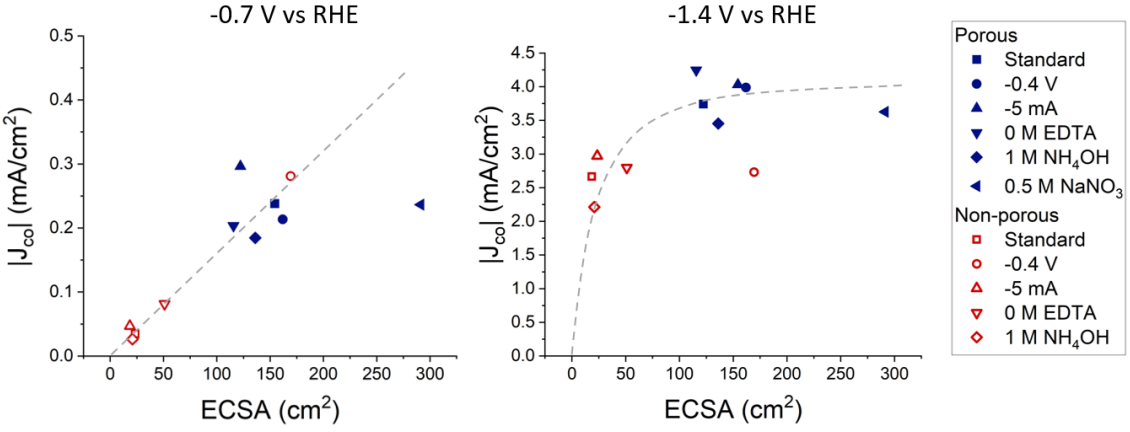

Figure 4.8: j_{CO} at -0.7 and -1.4 V vs RHE plotted against ECSA for all porous (blue, filled) and non-porous (red, open) samples. The symbols indicate the synthesis conditions and the grey dashed lines are a guide for the eye.

An observation that can be made, is that the order of highest to lowest j_{CO} within porous and non-porous samples are similar. To illustrate, from a low to high j_{CO} at -1.4 V vs RHE, the order is 1 M NH_4OH, Standard, -0.4 V, -5 mA, and 0 M EDTA for porous Ag. For non-porous Ag, this order is 1 M NH_4OH, Standard, -0.4 V, 0 M EDTA, and -5 mA. This might indicate that the facet-dependent structure-performance relationship of the non-porous Ag morphology is partially retained after introducing porosity, with the additional benefit of a higher surface area. In other words, these findings might suggest that the morphology surrounding pores contributes to the catalytic performance of porous Ag.

However, the possible interference of non-porous regions in porous catalysts, as shown in the supplementary information Section A.10, can not be ruled out. Usually, it is argued that the surface area of the non-porous regions is negligible compared to the surface area of the porous regions. But in this case, the plot of j_{CO} against ECSA at -1.4 V vs RHE in Figure 4.8 shows that at this potential there is no linear correlation between the two anymore. Specifically, the (non-porous) samples with a relatively low surface area show CO_2 conversion at almost the same rate as the (porous) samples with a high surface area. For instance, j_{CO} of the Standard sample only increases with a factor of 1.4 as a result of porosity when compared to the non-porous Standard sample, or 0.21 when j_{CO} is normalized by the ECSA (Supplementary A.11). This indicates that at high overpotentials the porous catalysts might suffer from internal mass transport limitations or porosity-induced ohmic drop effects that effectively leave the bottom part of the pore structure electrochemically inactive.[53] All combined, it is probable that the observed non-porous regions contribute to the catalytic performance of the porous catalysts, but the extent is undefined. Future investigations should therefore eliminate these non-porous regions by implementing a modified templating approach.

Another source of uncertainty is the lack of information about reproducibility. It has not been established when a difference in j_{CO} values between porous samples is significant. The synthesis and catalysis have only been repeated for one synthesis condition, as shown in the supplementary information Section A.12, but this is not sufficient for proper statistical analysis. Therefore, while it is clear that at -0.7 V vs RHE the enhanced CO_2 conversion is a result of the increased surface area, the effect of the morphology around the porosity is undetermined.

So far this section has focused on the activity toward CO production. Now it is time to consider the effect of porosity and morphology on the activity towards the Hydrogen Evolution Reaction (HER). This is a competing side reaction for electrochemical CO_2 reduction in aqueous systems, so a low hydrogen partial current density (j_{H2}) is beneficial. Figure 4.9 shows the j_{H2} of all porous and non-porous Ag catalysts, grouped by their structure (flat or coral-like). Before classifying the samples by structure, it seemed like no clear effect of the porosity was present, as at - 1.4 V vs RHE, j_{H_2} ranges from 0.12 to 0.51 for porous Ag, and from 0.16 to 0.70 for non-porous catalysts. However, this closer examination reveals that compared to non-porous Ag, j_{H2} is decreased for porous systems with a flat structure (Standard, - 5 mA, and 1 M NH_4OH), and increased for porous catalysts with a coral-like structure (-0.4 V, 0 M EDTA). For example, at -1.4 V vs RHE j_{H2} decreases from 0.60 to 0.39 for the Standard sample, and increases from 0.28 to 0.51 for the -0.4 V sample after introducing porosity. This is likely a result of improved mass transport in the hierarchical pore system in coral-like structures, as explained by DLC results

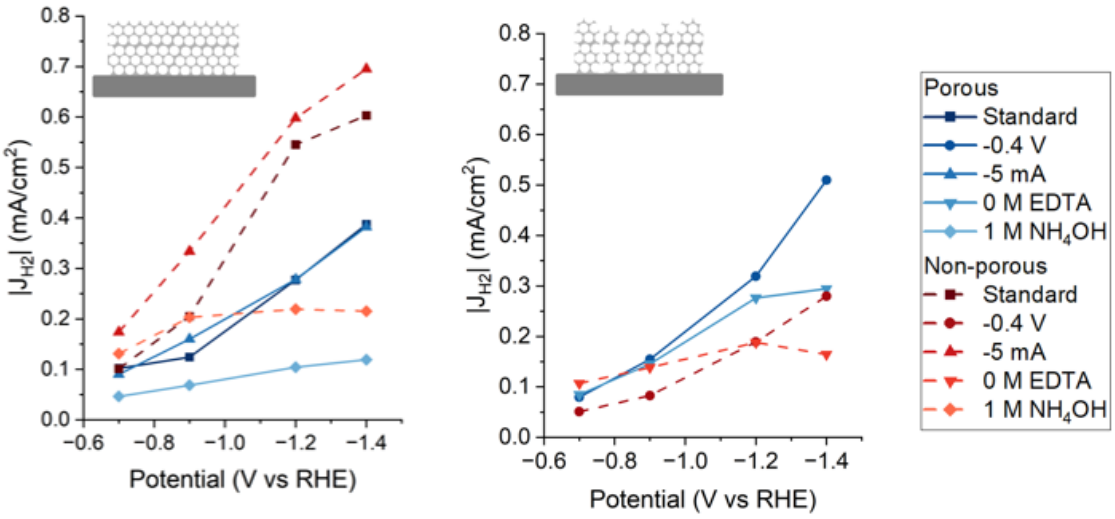

Figure 4.9: H_2 partial current densities of all porous (blue) and non-porous (red, dashed) samples, grouped by their structure (flat or coral-like). The symbols indicate the synthesis conditions.

in the next paragraph.

DLC measurements at a wide range of scan rates were done for the porous 0 M EDTA, -0.5 M $NaNO_3$, and 1 M NH_4OH catalysts. In the plot of the anodic capacitive current versus the scan rates (0.005 - 1 V/s) presented in Figure 4.10, it can be seen that the sample with the coral-like structure (0 M EDTA) has a linear progression, while the flat sample (1 M NH_4OH) plateaus. The latter progression was also found for the other measured flat structure (0.5 M $NaNO_3$) and is probably a result of ion transport limitations.[29,54] Therefore, the porous structure

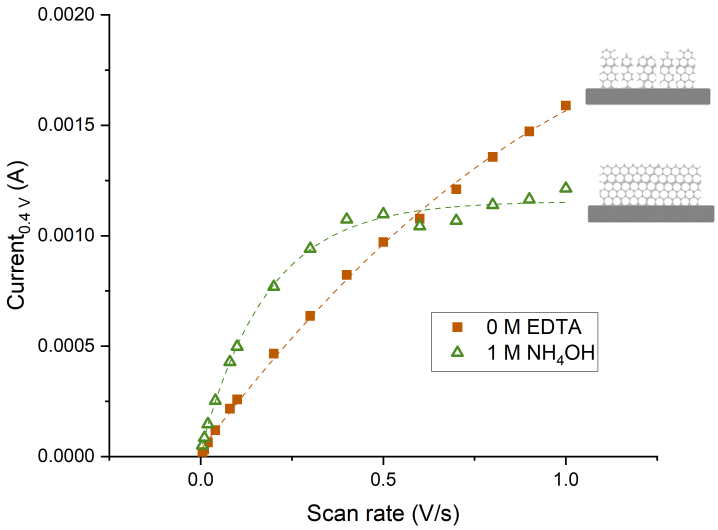

Figure 4.10: Anodic currents at 0.4 V vs RHE of DLC measurements of 1 M NH_4OH (green, flat) and 0 M EDTA (brown, coral-like) at a wide range of scan rates (0.005 - 1 V/s), with dashed lines to guide the eye.

induces low ion diffusion capabilities for the flat 0.5 M $NaNO_3$ and 1 M NH_4OH

catalysts. These results are in accordance with the study on inverse opal Ag (Ag-IO) for CO_2 reduction by Yoon et al., where it was found that mesostructure-induced transport limitations impede the HER for Ag.[23] On the contrary, for the coral-like 0 M EDTA, these diffusion limitations are not found, which is likely a consequence of its hierarchical pore structure. However, it is not clear why the additional macroporosity seemingly promotes the HER in porous coral-like structures (-0.4 V and 0 M EDTA). In addition, the reproducibility of the j_{H2} should be investigated in more depth (supplementary information Section A.12) in order to determine whether these morphological effects are significant.

4.1.2.3 Stability

Having discussed the selectivity and activity of porous Ag, this section will focus on the stability of the porous Ag structure. The post-catalytic structure of all porous Ag samples was determined with HR-SEM. Figure 4.11 compares the morphology of porous 0.5 M $NaNO_3$ before and after 2 cycles of catalysis. It is evident that the porosity remained, but the surface morphology appears smoothed. This smoothening was observed for all other samples as well, which is why it is interesting to investigate when this occurs.

In order to understand the restructuring process during catalysis, HR-SEM samples were obtained after each step in a model catalysis study, as shown in Figure 4.12. What can be observed, is that the morphology already becomes less sharp during CV. Applying potentials of -0.7 V and -0.9 V vs RHE does not seem to further smooth the structure, but after -1.2 V vs RHE, the structural change further progresses. It, therefore, appears the restructuring is potential-dependent, as the higher potentials are also applied during CV. In addition, these findings imply that the morphology tested during catalysis deviates from the morphology determined pre-catalysis.

When comparing the morphology after -1.4 V vs RHE to the structure after 2 cycles of catalysis (Figure 4.11), the main difference is that white dots are present on the sample from the model catalysis. Most likely, these are Pt nanoparticles, originating from the dissolution of the Pt wire and consequent redeposition at the cathode, as in the model catalysis they were not separated by a membrane like they are during a real catalytic test. However, the additional contrast the Pt particles cause in the HR-SEM image makes it hard to assess the structural changes during the second cycle of catalysis.

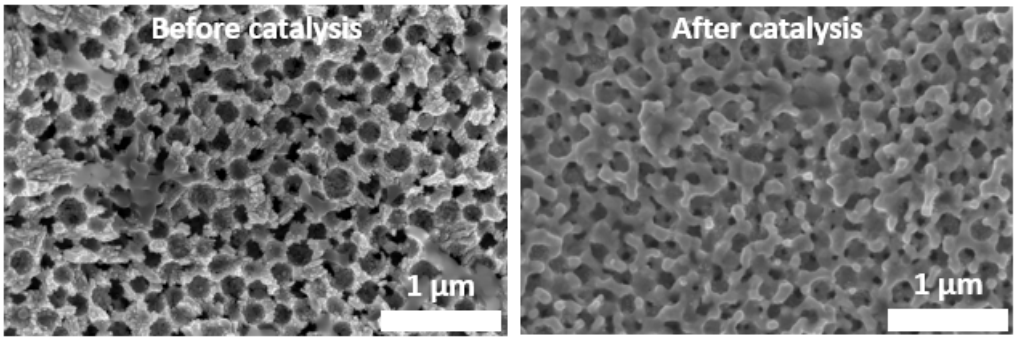

Figure 4.11: HR-SEM images of 0.5 M $NaNO_3$ before (left) and after 2 cycles of catalysis (right).

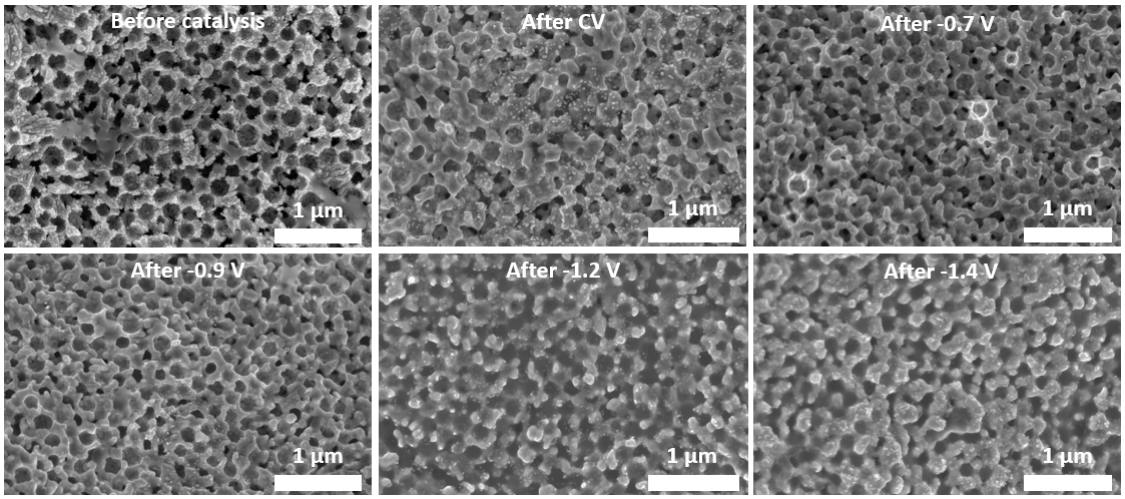

Figure 4.12: HR-SEM images of the porous 0.5 M $NaNO_3$ sample before catalysis, after CV, and after -0.7, -0.9, -1.2 and -1.4 V vs RHE

The stability-related performance of porous Ag was investigated by running 3 cycles of catalysis. However, only on a porous -0.4 V sample where half of the electrode was covered with tape, this was possible. For all the other samples, the measurement stopped prior to the end of the third cycle, which is likely an effect of electrolyte saturation or membrane deactivation. The activity towards CO during these 3 cycles is shown in Figure 4.13. It is clear that the activity increases for each cycle, reporting j_{CO} values of -1.84, 2.22, and 2.48 mA/cm^2 at -1.4 V vs RHE for cycles 1, 2, and 3, respectively. However, the morphological changes that occur during the second and third cycles have not been established. As a result, it is hard to discern if the rising activity is an effect of structural changes in the catalyst, or a change in the electrolyte composition. It might be that a changing electrolyte causes a lower resistance in the cell, which effectively means a slightly higher overpotential is applied, leading to a higher current. Therefore, the effect of the smoothening of porous Ag on CO_2 reduction is yet to be determined.

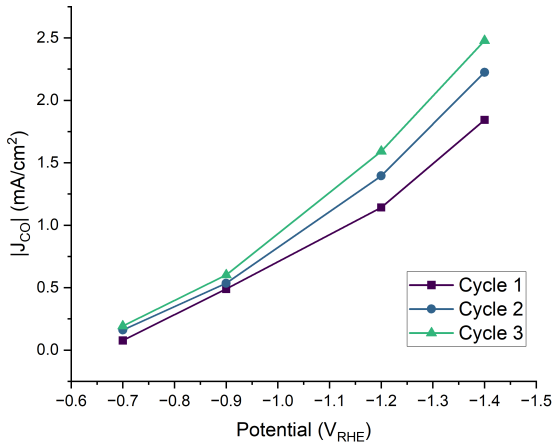

Figure 4.13: CO partial current density during 3 cycles of catalysis of the porous -0.4 V sample where half of the electrode is covered in tape.

4.2 Exploratory research: Porous Ag-Cu

So far, the focus of this work has been on porous Ag. In order to explore the full potential of the template-based synthesis, a bimetallic Ag-Cu and a Cu catalyst were prepared on Ag foil via this route. For the bimetallic Ag-Cu catalyst, a small amount of Cu was deposited on top of Ag because preliminary research found that codeposition of Ag-Cu was not possible in the porous structure (supplementary information Section A.4).

4.2.1 Morphology and composition

To establish whether the synthesis route was successful for Cu and Ag-Cu, the morphology and composition of the catalysts were determined with HR-SEM (Figure 4.14) and EDX. Strikingly, the Cu catalyst did not demonstrate porosity, despite using a PMMA sphere template. Likewise, the Ag-Cu sample consists of 1.4 wt% non-porous Cu crystals on top of a porous Ag structure. It appears that the specific synthesis conditions do not allow the Cu to grow around the template, so the method is not as versatile as expected. In literature, several successful Cu inverse opals have been synthesized using similar strategies, so a slight adaptation of the synthesis route might still allow the production of porous Cu or Ag-Cu.[55,56]

4.2.2 Selectivity

Now the morphology and composition of the Cu-containing catalysts are known, it is interesting to see how this affects the selectivity for CO_2 reduction. In Figure 4.15, the product faradaic efficiencies (FE) of Standard porous Ag, porous Ag-Cu, and Cu at -1.4 V vs RHE are shown. Interestingly, the addition of 1.4 wt% of Cu on Ag, already steered the product selectivity from just CO and H_2 for Ag, to CO, ethene, methane, formate, ethanol, acetate, and H_2 for Ag-Cu.

When comparing Ag-Cu to Cu, immediately a decrease in the H_2 selectivity and an increase in CO selectivity can be observed by the presence of porous Ag. More strikingly, ethanol and acetate are formed on Ag-Cu, but not when only Cu is used. Similar trends are encountered in literature, as multiple studies on bimetallic Cu systems with a CO-forming metal such as Ag or Au, have found increased activity towards acetate.[32] These results are often attributed to a tandem catalyst scheme where CO is formed on Ag or Cu, and subsequently adsorbed on the Cu surface,

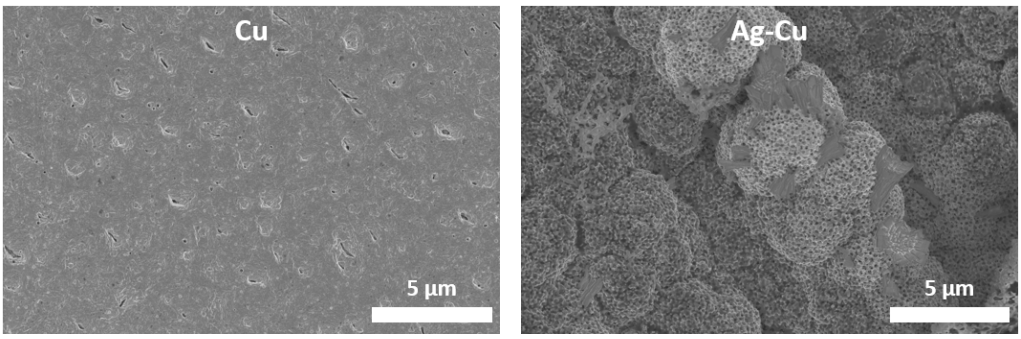

Figure 4.14: HR-SEM images of the Cu (left) and the Ag-Cu (right) sample

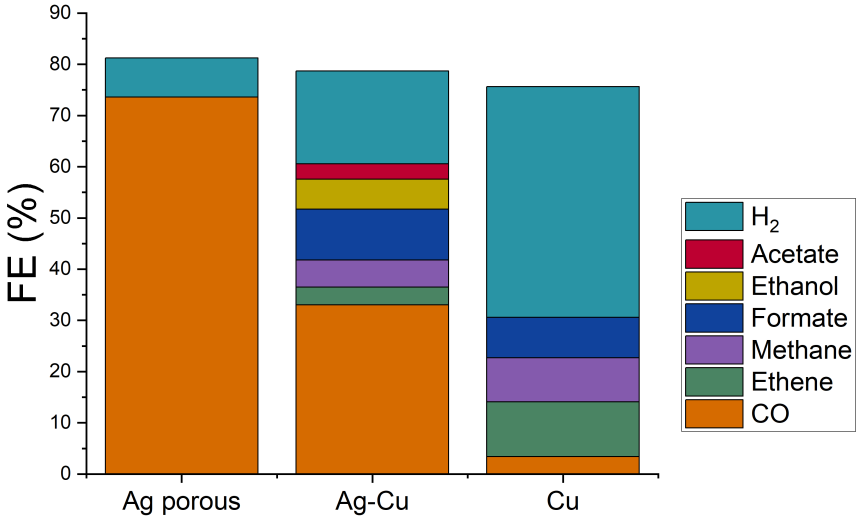

Figure 4.15: Product faradaic efficiencies of Standard porous Ag (left), Ag-Cu (middle) and Cu (right) for CO_2 reduction.

where it is further converted to acetate.[32] All in all, it is remarkable that such a small amount of Cu can drastically change the selectivity.

Chapter 5

Conclusion and outlook

In conclusion, this work provides a novel method to study the effect of porosity on different Ag morphologies. Specifically, we have developed a template-based synthesis route of porous Ag that enables the introduction of well-defined porosity to a variety of Ag morphologies. We demonstrated that for certain Ag morphologies, porous samples reached higher CO and lower H_2 faradaic efficiencies compared to their non-porous counterpart in agreement with previous studies. However, for the remaining morphologies this trend was inverted or absent, an observation not yet reported in literature. The CO_2 to CO conversion activity was mainly promoted by the porosity in all of the prepared Ag morphologies. We have revealed that this is predominantly an effect of the higher surface area, as at -0.7 V vs RHE a linear correlation between the j_{CO} and the electrochemical surface area was found. While morphological effects were explored for the activity towards CO, the analysis was limited by non-porous regions in porous Ag catalysts. Moreover, we have for the first time uncovered that porosity-induced HER suppression is lost for coral-like Ag structures, likely as a result of improved ion transport conditions. It is noteworthy that the porosity remained stable after 2 cycles of catalysis. Lastly, exploratory research has demonstrated that the deposition of a small amount of Cu on porous Ag can drastically change the selectivity to products beyond CO.

Future research would benefit from using a similar research approach on a homogeneous and highly ordered colloidal crystal template. This would allow the findings of the research to be translated to previously reported model studies on porous catalysts for CO_2 reduction. In addition, the elimination of non-porous regions in porous Ag catalysts would enable a proper investigation of morphological effects in porous Ag. Lead underpotential deposition would provide an additional method of determining the catalyst surface area. Moreover, it would be interesting to repeat the experiments on a flat non-Ag substrate, in order to be able to improve the assessment of the Ag morphology with XRD. Due to the importance of mass transport conditions for porous catalysts, catalysis with rotating ring disk electrodes could potentially be insightful. Moreover, to better understand the catalyst stability, it would be interesting to perform catalysis on a post-catalysis sample and to run long-duration catalysis (e.g. 3 days) in a flow cell. Once these experiments have been addressed, another promising line of research would be to further explore this method for other metals and bimetallic systems. All of these findings will contribute to a more fundamental understanding of porous catalysts for CO_2 reduction.

Layman's abstract

The high amount of carbon dioxide (CO_2) that's currently in the atmosphere causes global warming, which is a big problem. That's why we want to produce less CO_2. When chemicals and fuels are made from oil, they emit a lot of CO_2 into the atmosphere. It would be better to collect CO_2 from the atmosphere and turn it into chemicals and fuels. To do that, we need a catalyst that for example converts CO_2 into carbon monoxide (CO). CO can then be used to produce fuels with processes that already exist. One catalyst that can make CO from CO_2, is silver. It works even better when the silver has pores because it has a bigger surface. There might also be other factors that make porous silver a better catalyst than normal silver. What we know about silver in general, is that its structure determines how much CO_2 we convert as well. However, we don't know what adding pores does to every silver structure. That's why we have investigated the effect of pores in different silver shapes. We have discovered that the effect of adding pores is different for different silver structures. This information will help us make better catalysts for CO_2 conversion and work towards a more sustainable future.

Acknowledgements

I would like to thank several people who have had valuable contributions to my master's project. First and foremost, I want to thank my daily supervisor Maaike van Ittersum. Without her amazing project proposal, guidance, and useful discussion this thesis would not exist. Then I want to express my gratitude to prof. dr. Petra de Jongh and dr. Peter Ngene for welcoming me to the Materials Chemistry and Catalysis group and providing useful feedback and suggestions. Next, I want to acknowledge Claudia Keijzer for performing HR-SEM on my samples, and Matt Peerlings for taking NMR measurements. Hans Meeldijk is also thanked for his EDX contributions, and Dennie Wezendonk and Jan Willem de Rijk are acknowledged for their technical assistance. Many people in the electrocatalysis group have helped me as well in the last year. I have had useful discussions with Valerio Gulino, Francesco Mattarozzi, and Matt Peerlings and received technical support from them. Also, fellow students Mei-Ju Goemans and Alexander Flick have contributed in the lab. In addition, I want to thank Henrik Rodenburg for his contributions to my Python scripts. Last but not least, I want to thank the whole MCC group for creating a nice working environment.

Bibliography

[1] M. Masson-Delmotte, V., P. Zhai, A. Pirani, S.L. Connors, C. Péan, S. Berger, N. Caud, Y. Chen, L. Goldfarb, M.I. Gomis, K. Huang, E. Leitzell, T. Lonnoy, J.B.R. Matthews, T.K. Maycock, O. Waterfield, R. Yelekçi, R. Yu, and B. Zhou, *IPCC, 2021: Summary for Policymakers. In: Climate Change 2021: The Physical Science Basis. Contribution of Working Group I to the Sixth Assessment Report of the Intergovernmental Panel on Climate Change*. Cambridge University Press.

[2] Z. Sun, T. Ma, H. Tao, Q. Fan, and B. Han, "Fundamentals and Challenges of Electrochemical CO_2 Reduction Using Two-Dimensional Materials," *Chem*, vol. 3, no. 4, pp. 560–587, 2017.

[3] Q. Lu and F. Jiao, "Electrochemical CO_2 reduction: Electrocatalyst, reaction mechanism, and process engineering," *Nano Energy*, vol. 29, pp. 439–456, 2016.

[4] L. Xie, J. Liang, C. Priest, T. Wang, D. Ding, G. Wu, and Q. Li, "Engineering the atomic arrangement of bimetallic catalysts for electrochemical CO_2 reduction," *Chemical Communications*, vol. 57, no. 15, pp. 1839–1854, 2021.

[5] W. Zhu, B. M. Tackett, J. G. Chen, and F. Jiao, "Bimetallic Electrocatalysts for CO_2 Reduction," 2018.

[6] Y. Wang, L. Cao, N. J. Libretto, X. Li, C. Li, Y. Wan, C. He, J. Lee, J. Gregg, H. Zong, D. Su, J. T. Miller, T. Mueller, and C. Wang, "Ensemble Effect in Bimetallic Electrocatalysts for CO_2 Reduction," *Journal of the American Chemical Society*, vol. 141, no. 42, pp. 16635–16642, 2019.

[7] A. Bagger, W. Ju, A. S. Varela, P. Strasser, and J. Rossmeisl, "Electrochemical CO_2 Reduction: A Classification Problem," *ChemPhysChem*, vol. 18, no. 22, pp. 3266–3273, 2017.

[8] J. He, N. J. Johnson, A. Huang, and C. P. Berlinguette, "Electrocatalytic Alloys for CO_2 Reduction," *ChemSusChem*, vol. 11, no. 1, pp. 48–57, 2018.

[9] Q. Lu, J. Rosen, Y. Zhou, G. S. Hutchings, Y. C. Kimmel, J. G. Chen, and F. Jiao, "A selective and efficient electrocatalyst for carbon dioxide reduction," *Nature Communications*, vol. 5, 2014.

[10] D. Sun, X. Xu, Y. Qin, S. P. Jiang, and Z. Shao, "Rational Design of Ag-Based Catalysts for the Electrochemical CO_2 Reduction to CO: A Review," *ChemSusChem*, vol. 13, no. 1, pp. 39–58, 2020.

[11] Q. Yu, C. Guo, J. Ge, Y. Zhao, Q. Liu, P. Gao, J. Xiao, and H. Li, "Morphology controlling of silver by plasma engineering for electrocatalytic carbon dioxide reduction," *Journal of Power Sources*, vol. 453, no. February, p. 227846, 2020.

[12] S. A. Mahyoub, F. A. Qaraah, C. Chen, F. Zhang, S. Yan, and Z. Cheng, "An overview on the recent developments of Ag-based electrodes in the electrochemical reduction of CO_2 to CO," *Sustainable Energy and Fuels*, vol. 4, no. 1, pp. 50–67, 2019.

[13] E. L. Clark, S. Ringe, M. Tang, A. Walton, C. Hahn, T. F. Jaramillo, K. Chan, and A. T. Bell, "Influence of Atomic Surface Structure on the Activity of Ag for the Electrochemical Reduction of CO_2 to CO," *ACS Catalysis*, vol. 9, no. 5, pp. 4006–4014, 2019.

[14] X. Min, H. Lv, Y. Yamauchi, and B. Liu, "Porous metal nanocrystal catalysts: Can crystalline porosity enable catalytic selectivity?," *CCS Chemistry*, vol. 4, no. 6, pp. 1829–1842, 2022.

[15] H. Wang, Z. Han, L. Zhang, C. Cui, X. Zhu, X. Liu, J. Han, and Q. Ge, "Enhanced CO selectivity and stability for electrocatalytic reduction of CO_2 on electrodeposited nanostructured porous Ag electrode," *Journal of CO_2 Utilization*, vol. 15, pp. 41–49, 2016.

[16] A. Goyal, G. Marcandalli, V. A. Mints, and M. T. Koper, "Competition between CO_2 Reduction and Hydrogen Evolution on a Gold Electrode under Well-Defined Mass Transport Conditions," *Journal of the American Chemical Society*, vol. 142, no. 9, pp. 4154–4161, 2020.

[17] D. Kang, T. W. Kim, S. R. Kubota, A. C. Cardiel, H. G. Cha, and K. S. Choi, "Electrochemical Synthesis of Photoelectrodes and Catalysts for Use in Solar Water Splitting," *Chemical Reviews*, vol. 115, no. 23, pp. 12839–12887, 2015.

[18] Y. Jeon, S. Choe, H. C. Kim, M. J. Kim, and J. J. Kim, "Electrodeposition of Cu-Ag films in ammonia-based electrolyte," *Journal of Alloys and Compounds*, vol. 775, pp. 639–646, 2019.

[19] A. Liu, X. Ren, M. An, J. Zhang, P. Yang, B. Wang, Y. Zhu, and C. Wang, "A Combined Theoretical and Experimental Study for Silver Electroplating," *Scientific Reports*, vol. 4, pp. 35–43, 2015.

[20] G. M. De Oliveira, L. L. Barbosa, R. L. Broggi, and I. A. Carlos, "Voltammetric study of the influence of EDTA on the silver electrodeposition and morphological and structural characterization of silver films," *Journal of Electroanalytical Chemistry*, vol. 578, no. 1, pp. 151–158, 2005.

[21] T. S. Mkwizu, M. K. Mathe, and I. Cukrowski, "Multilayered Nanoclusters of Platinum and Gold: Insights on Electrodeposition Pathways, Electrocatalysis, Surface and Bulk Compositional Properties," *Journal of The Electrochemical Society*, vol. 160, no. 9, pp. H529–H546, 2013.

[22] Z. Yan, H. Liu, Z. Hao, M. Yu, X. Chen, and J. Chen, "Electrodeposition of (hydro)oxides for an oxygen evolution electrode," *Chemical Science*, vol. 11, no. 39, pp. 10614–10625, 2020.

[23] Y. Yoon, A. S. Hall, and Y. Surendranath, "Tuning of Silver Catalyst Mesostructure Promotes Selective Carbon Dioxide Conversion into Fuels," *Angewandte Chemie - International Edition*, vol. 55, no. 49, pp. 15282–15286, 2016.

[24] P. T. Kissinger and A. W. Bott, "Electrochemistry for the Non-Electrochemist," *Current Separations*, vol. 20, no. 2, pp. 51–53, 2002.

[25] N. Elgrishi, K. J. Rountree, B. D. McCarthy, E. S. Rountree, T. T. Eisenhart, and J. L. Dempsey, "A Practical Beginner's Guide to Cyclic Voltammetry," *Journal of Chemical Education*, vol. 95, no. 2, pp. 197–206, 2018.

[26] S. Liang, N. Altaf, L. Huang, Y. Gao, and Q. Wang, "Electrolytic cell design for electrochemical CO_2 reduction," *Journal of CO_2 Utilization*, vol. 35, no. September 2019, pp. 90–105, 2020.

[27] P. Atkins, J. de Paulo, and J. Keeler, *Physical chemistry*. Oxford University Press, 11 ed., 2018.

[28] A. C. Fisher, *Electrode dynamics*, vol. 1. Oxford University Press Oxford, 1996.

[29] D. M. Morales and M. Risch, "Seven steps to reliable cyclic voltammetry measurements for the determination of double layer capacitance," *JPhys Energy*, vol. 3, no. 3, 2021.

[30] P. Connor, J. Schuch, B. Kaiser, and W. Jaegermann, "The Determination of Electrochemical Active Surface Area and Specific Capacity Revisited for the System MnOx as an Oxygen Evolution Catalyst," *Zeitschrift fur Physikalische Chemie*, vol. 234, no. 5, pp. 979–994, 2020.

[31] C. Batchelor-McAuley, "Defining the Onset Potential," *Current Opinion in Electrochemistry*, vol. 37, p. 101176, 2022.

[32] S. Nitopi, E. Bertheussen, S. B. Scott, X. Liu, A. K. Engstfeld, S. Horch, B. Seger, I. E. Stephens, K. Chan, C. Hahn, J. K. Nørskov, T. F. Jaramillo, and I. Chorkendorff, "Progress and Perspectives of Electrochemical CO_2 Reduction on Copper in Aqueous Electrolyte," *Chemical Reviews*, vol. 119, no. 12, pp. 7610–7672, 2019.

[33] G. Wen, B. Ren, Y. Zheng, M. Li, C. Silva, S. Song, Z. Zhang, H. Dou, L. Zhao, D. Luo, A. Yu, and Z. Chen, "Engineering Electrochemical Surface for Efficient Carbon Dioxide Upgrade," *Advanced Energy Materials*, vol. 12, no. 3, pp. 1–40, 2022.

[34] Y. Y. Birdja, E. Pérez-Gallent, M. C. Figueiredo, A. J. Göttle, F. Calle-Vallejo, and M. T. Koper, "Advances and challenges in understanding the electrocatalytic conversion of carbon dioxide to fuels," 2019.

[35] Z. Chen, G. Zhang, H. Chen, J. Prakash, Y. Zheng, and S. Sun, "Multi-metallic catalysts for the electroreduction of carbon dioxide: Recent advances and perspectives," *Renewable and Sustainable Energy Reviews*, vol. 155, no. November 2021, p. 111922, 2022.

[36] A. R. Woldu, Z. Huang, P. Zhao, L. Hu, and D. Astruc, "Electrochemical CO_2 reduction (CO_2RR) to multi-carbon products over copper-based catalysts," *Coordination Chemistry Reviews*, vol. 454, p. 214340, 2022.

[37] Y. Hori, H. Wakabe, T. Tsukamoto, and O. Koga, "Electrocatalytic process of CO selectivity in electrochemical reduction of CO_2 at metal electrodes in aqueous media," *Electrochimica Acta*, vol. 39, 1994.

[38] J. E. van den Reijen, P. H. Keijzer, and P. E. de Jongh, "Pore structure stabilization during the preparation of single phase ordered macroporous α-alumina," *Materialia*, vol. 4, no. September, pp. 423–430, 2018.

[39] A. Stein, "Sphere templating methods for periodic porous solids," *Microporous and Mesoporous Materials*, vol. 44-45, pp. 227–239, 2001.

[40] R. van Dommelen, P. Fanzio, and L. Sasso, "Surface self-assembly of colloidal crystals for micro- and nano-patterning," *Advances in Colloid and Interface Science*, vol. 251, pp. 97–114, 2018.

[41] C. Y. Kuo and S. Y. Lu, "Fabrication of patterned inverse opal structure through physical confinement assembly and selective electrochemical deposition," *Journal of the American Ceramic Society*, vol. 90, no. 6, pp. 1956–1958, 2007.

[42] J. H. Han, A. V. Shneidman, D. Y. Kim, N. J. Nicolas, J. E. van der Hoeven, M. Aizenberg, and J. Aizenberg, "Highly Ordered Inverse Opal Structures Synthesized from Shape-Controlled Nanocrystal Building Blocks," *Angewandte Chemie - International Edition*, vol. 61, no. 3, pp. 1–9, 2022.

[43] J. Meng, X. Li, M. Qin, Y. Pei, S. Yang, Y. Lan, R. Wang, and G. Chen, "Effects of pore size of reverse opal structured PEDOT films on their electrochromic performances," *Organic Electronics*, vol. 50, pp. 16–24, 2017.

[44] S. S. V. Tatiparti and F. Ebrahimi, "Potentiostatic versus galvanostatic electrodeposition of nanocrystalline Al-Mg alloy powders," *Journal of Solid State Electrochemistry*, vol. 16, no. 3, pp. 1255–1262, 2012.

[45] F. Nasirpouri, *Fundamentals and principles of electrode-position*, vol. 62. 2017.

[46] L. Guo and P. C. Searson, "On the influence of the nucleation overpotential on island growth in electrodeposition," *Electrochimica Acta*, vol. 55, no. 13, pp. 4086–4091, 2010.

[47] M. G. Korporaal, "Bachelorthesis: Template based silver catalysts for the electrochemical reduction of CO_2," 2021.

[48] R. Schroden, N. Balakrishnan, A. Stein, and M. Ward, "Inverse Opal Photonic Crystals A Laboratory Guide," *University of Minnesota, Materials Research Science and Engineering Center, Minnesota*, pp. 1–42, 2001.

[49] G. M. De Oliveira and I. A. Carlos, "Silver-copper electrodeposition from ammonium hydroxide solution: Influence of EDTA and HEDTA," *Journal of Applied Electrochemistry*, vol. 39, no. 8, pp. 1217–1227, 2009.

[50] S. Niu, S. Li, Y. Du, X. Han, and P. Xu, "How to reliably report the overpotential of an electrocatalyst," *ACS Energy Letters*, vol. 5, no. 4, pp. 1083–1087, 2020.

[51] A. S. Hall, Y. Yoon, A. Wuttig, and Y. Surendranath, "Mesostructure-induced selectivity in co$_2$ reduction catalysis," *Journal of the American Chemical Society*, vol. 137, no. 47, pp. 14834–14837, 2015.

[52] J. Y. Park, W. J. Dong, and J. L. Lee, "Monolithic Cl-Modified Nanoporous Ag Nanowires for Electrochemical CO_2 Reduction to CO," *ACS Applied Energy Materials*, vol. 5, no. 2, pp. 1627–1634, 2022.

[53] A. Goyal, C. J. Bondue, M. Graf, and M. T. Koper, "Effect of pore diameter and length on electrochemical co$_2$ reduction reaction at nanoporous gold catalysts," *Chemical Science*, vol. 13, no. 11, pp. 3288–3298, 2022.

[54] H. Wang and L. Pilon, "Physical interpretation of cyclic voltammetry for measuring electric double layer capacitances," *Electrochimica Acta*, vol. 64, pp. 130–139, 2012.

[55] X. Zheng, J. Han, Y. Fu, Y. Deng, Y. Liu, Y. Yang, T. Wang, and L. Zhang, "Highly efficient CO_2 reduction on ordered porous Cu electrode derived from Cu2O inverse opals," *Nano Energy*, vol. 48, no. March, pp. 93–100, 2018.

[56] M. T. Barako, J. M. Weisse, S. Roy, T. Kodama, T. J. Dusseault, M. Motoyama, M. Asheghi, F. B. Prinz, X. Zheng, and K. E. Goodson, "Thermal conduction in nanoporous copper inverse opal films," *Thermomechanical Phenomena in Electronic Systems -Proceedings of the Intersociety Conference*, pp. 736–743, 2014.

Appendix A

Supplementary information

For preliminary research presented in this appendix, SEM and EDX measurements were generally performed on the Phenom ProX from Thermofisher with acceleration voltages of 5, 10 or 15 kV.

A.1 PMMA template on Ag foil

When preparing a PMMA template on Ag foil, directly putting a PMMA suspension on Ag foil is not sufficient. Preliminary experiments showed that the template not sticks to the Ag foil substrate then. Several strategies were performed to overcome this obstacle. First, the PMMA suspension was diluted to 1 % w/w. With this diluted suspension, both nafion and P-123 were tested as binders. P-123 had been previously used in literature, but it was found in this study that it was only sufficient for a thin layer/monolayer. Nafion did allow the adhesion of a 3D array of PMMA spheres. Investigation with SEM exposed that the binder influences the packing of spheres, as seen in Figure A.1. While P-123 caused a closer packing of spheres compared to a sample without binder, the nafion solution resulted in a more disordered packing. Note that in order to allow SEM investigations, a 10 nm Pt layer was added with sputter coating on the PMMA/PS samples.

When PS spheres were used, the effect of both diluting the PS suspension and adding nafion is even more profound, as seen in Figure A.2. Without dilution, PS

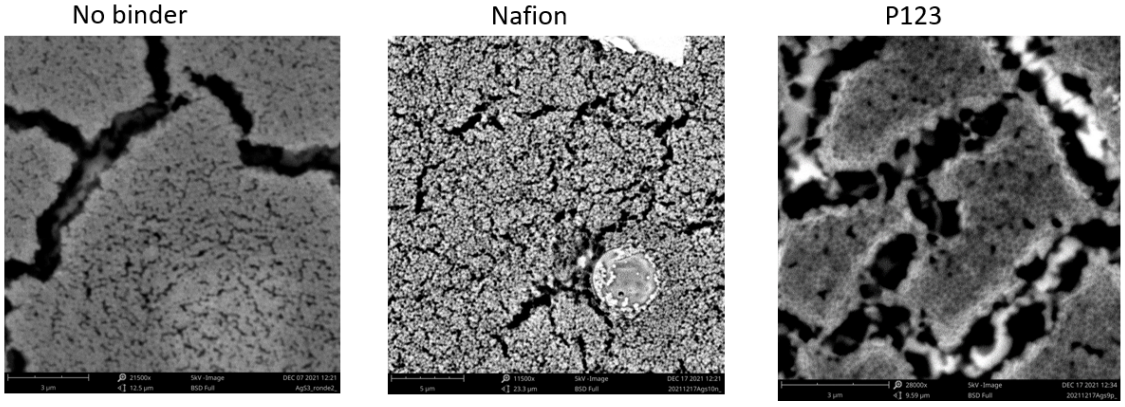

Figure A.1: SEM images of PMMA sphere without binder, with Nafion as a binder, and with P123 as a binder.

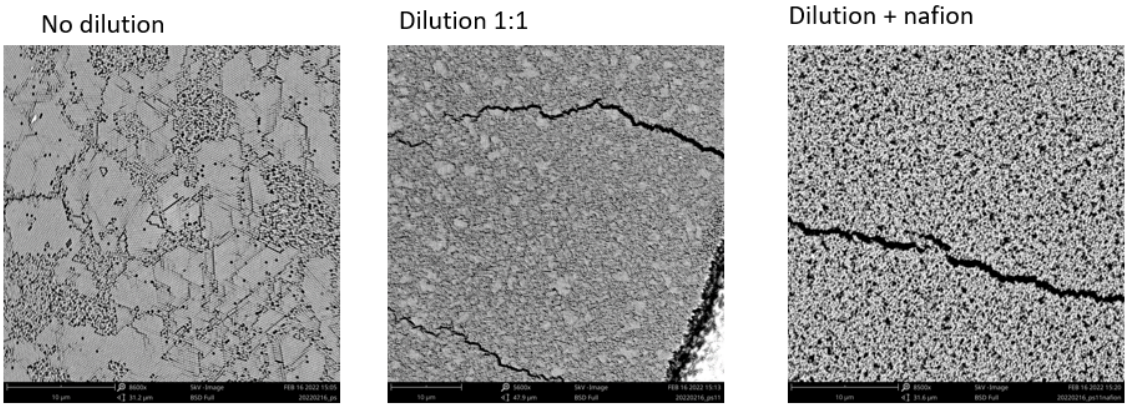

Figure A.2: SEM image of PS spheres on Ag foil without adaptations, diluted, and diluted+Nafion.

spheres have a close packing in a lot of regions. After dilution, most of these regions are gone, and only some very small regions remain. After dilution and addition of Nafion, the close packing is entirely gone, resulting in a disordered packing.

Lastly, it was found that the surface roughness of the silver foil was crucial for significant adhesion of the template. As seen in Figure A.3, when the Ag foil is completely smooth, an even layer of PMMA is formed, however, it quickly falls off the substrate. When the Ag foil has rough wrinkles, the PMMA remains on the substrate. However, the surface coverage and layer thickness are uneven, so a second layer was necessary for full surface coverage. When the Ag foil is finely wrinkled, the PMMA stays on the Ag foil, and an even layer is formed.

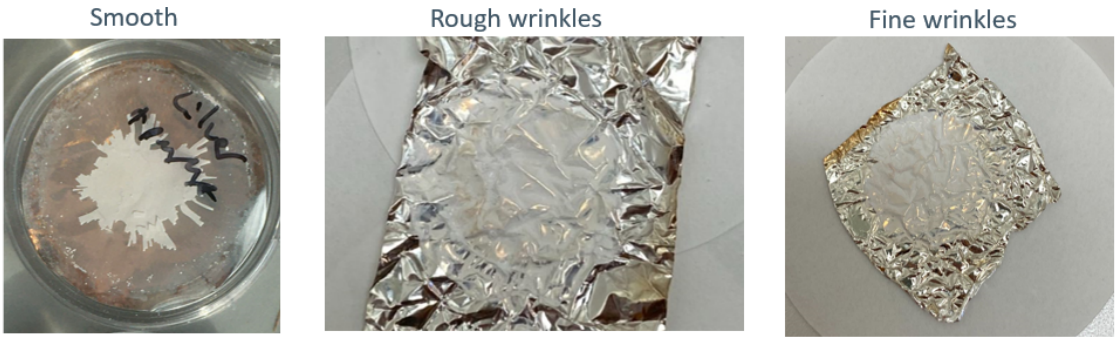

Figure A.3: PMMA on smooth, roughly wrinkled, and finely wrinkled Ag foil

Interestingly, when comparing the final structure of porous silver on Ag foil to porous silver on carbon paper (Figure A.4), it is apparent that the pores on carbon paper are much more open and accessible. This might be a result of the addition of Nafion to PMMA on Ag foil.

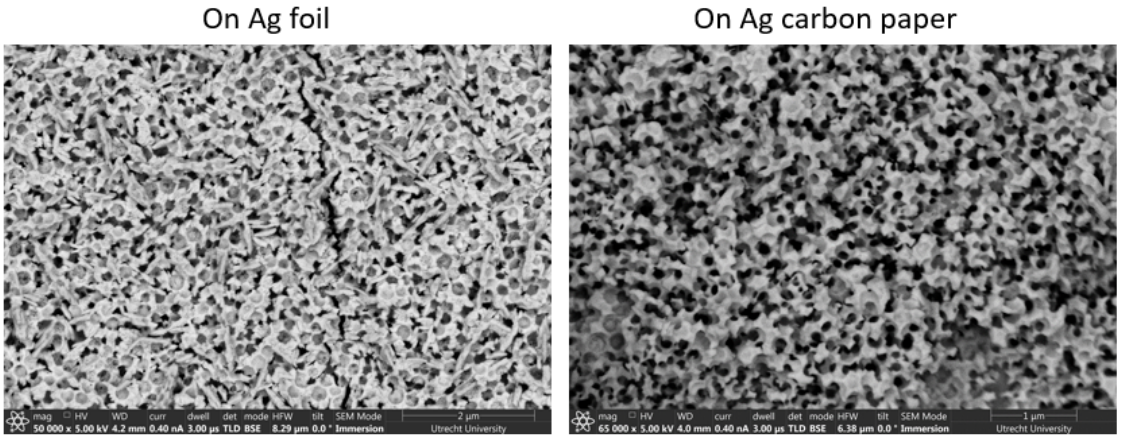

Figure A.4: HR-SEM images of Porous silver on Ag foil and carbon paper.

A.2 Stirring electrodeposition

As electrodeposition is dependent on mass transport at most potentials, agitation can be a crucial parameter. In the used setup, it could not be ensured that the stirring would be constant for all of the samples, which might be a problem for reproducibility. For that reason, the most reproducible option was to operate without the agitation of a stirring bean. Note that generally in literature, the solution is stirred.

When we stopped stirring and the reference electrode was positiond with a fixed distance to the electrodeposition holder, the electrodeposition curves became a lot smoother and more reproducible (Figure A.5).

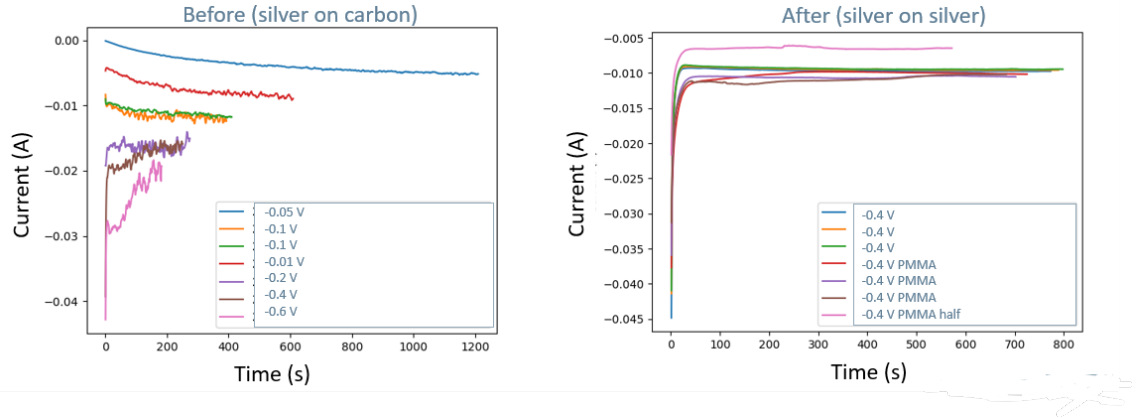

Figure A.5: Current vs time curves of electrodeposition of Ag on carbon with stirring (left), and Ag on Ag foil without stirring (right).

A.3 Effect potential

In literature, it was described that the deposit morphology depends on the potential.[45] To see what this entailed for Ag deposition, Ag was deposited on carbon paper at various potentials between 0.05 and -0.6 V vs Ag/AgCl. In Figure A.6 the

morphology changes are very clear, from cauliflower morphologies at low overpotentials to dendrites at high overpotentials. XRD was performed on -0.01 V and -0.4

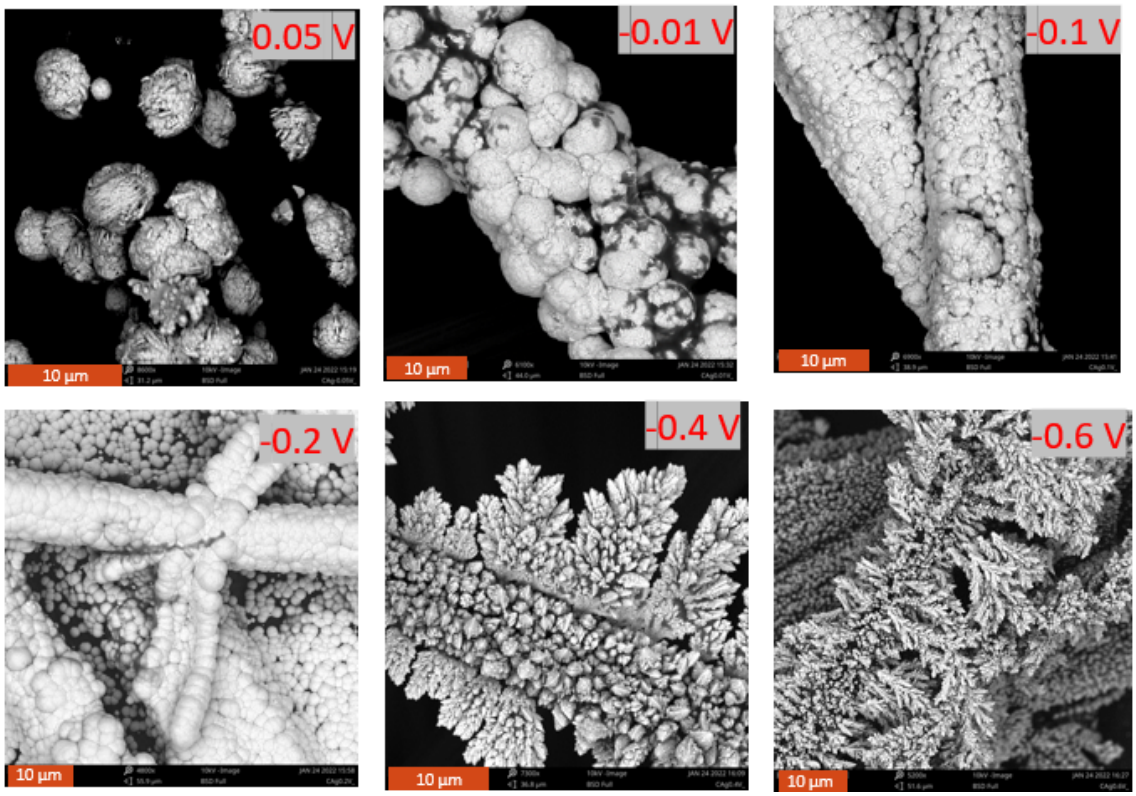

Figure A.6: SEM images of Ag deposited on carbon paper at potentials between 0.05 and -0.6 V vs Ag/AgCl.

V vs Ag/AgCl to see how much the facets changed (Figure A.7). By shifting -0.4 V slightly to the left, it is visible that -0.4 V has more 111 and 200 facets, and -0.01 V has more 220 and 311 facets.

A similar experiment was performed for Cu, but then between -0.38 V and -0.6 V . These potentials (also for Ag) were chosen based on the CV of the solution. Interestingly, at the lowest potential you can clearly see that electrodeposition is a nucleation and growth phenomenon. The Cu morphology is more spherical than Ag.

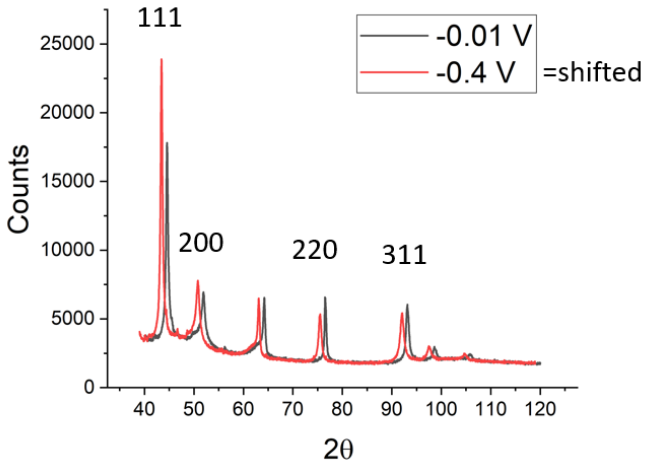

Figure A.7: XRD of Ag deposited at -0.01 V and -0.4 V (shifted slightly to the left)

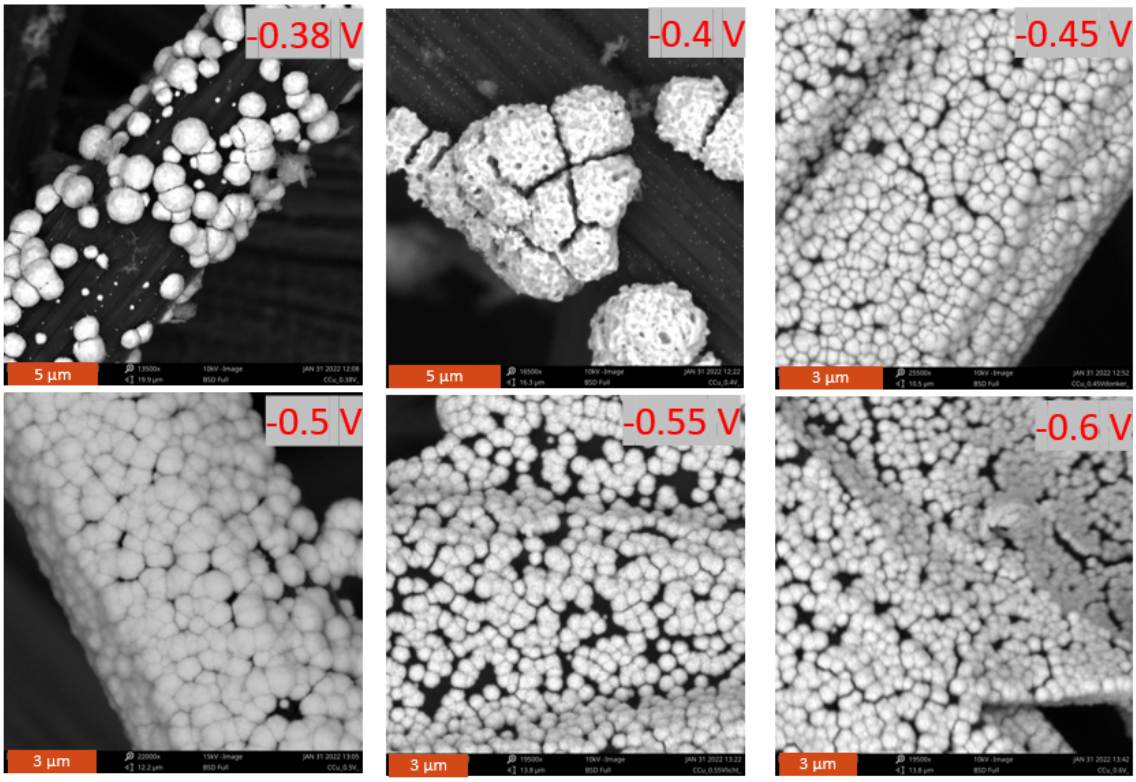

Figure A.8: SEM images of Cu deposited on carbon paper at potentials between -0.38 and -0.6 V vs Ag/AgCl.

A.4 Codeposition

In order to make a bimetallic Ag/Cu catalyst, codeposition of Ag and Cu was attempted based on the procedure of De Oliveira et al. on carbon paper.[49] A standard bath contained 0.1 M $Cu(NO_3)_2$, 0.05 M $AgNO_3$, 1 M $NaNO_3$, 0.5 M NH_4OH, and 0.01 M EDTA, but this resulted in precipitation of $Cu(OH)_2$, as seen in Figure A.9. Although codeposition was still possible with this solution, it is likely not reproducible.

Figure A.9: Precipitation of $Cu(OH)_2$ in standard codeposition solution.

The SEM images of Ag/Cu codeposition with the standard solution are presented in Figure A.10. Interestingly, the morphologies deviate from the Ag and Cu potentials at similar potentials. In addition, EDX mapping (Figure A.11) demonstrated that both Ag and Cu are present within one particle.

Comparing XRD of Ag -0.4 V, Cu -0.45 V, and Ag/Cu -0.45 V (Figure A.12) also shows the presence of both Ag and Cu. Only a very small peak shift of the Ag 110 peak (0.02 2θ) is observed, and the Cu 110 peak turned very broad. Note that these Cu samples were prepared in the solutions with precipitation.

In order to find a suitable codeposition solution, several bath parameters were changed, as shown in Table A.1. Most important was the NH_4OH concentration. With the standard 0.5 M NH_4OH, the solution had a high pH so OH_- ions precipitated with Cu_{2+}. Interestingly, if more NH_4OH is added, $Cu(NH_4OH)_4{}^{2+}$ complexes are formed that are soluble in water, and the solution turns a dark blue. That's why increasing the NH_4OH concentration managed to prevent precipitation. However, if too much NH_4OH was present, the Cu would not deposit anymore. For that reason, using 0.6125 M NH_4OH was the solution that enabled Ag/Cu codeposition.

When codeposition was attempted on Ag foil with a template, initially it seemed succesful.(Figure A.13) However, the allegedly porous metal was not stable enough, as it dispersed in acetone during PMMA dissolution. (Figure A.14)

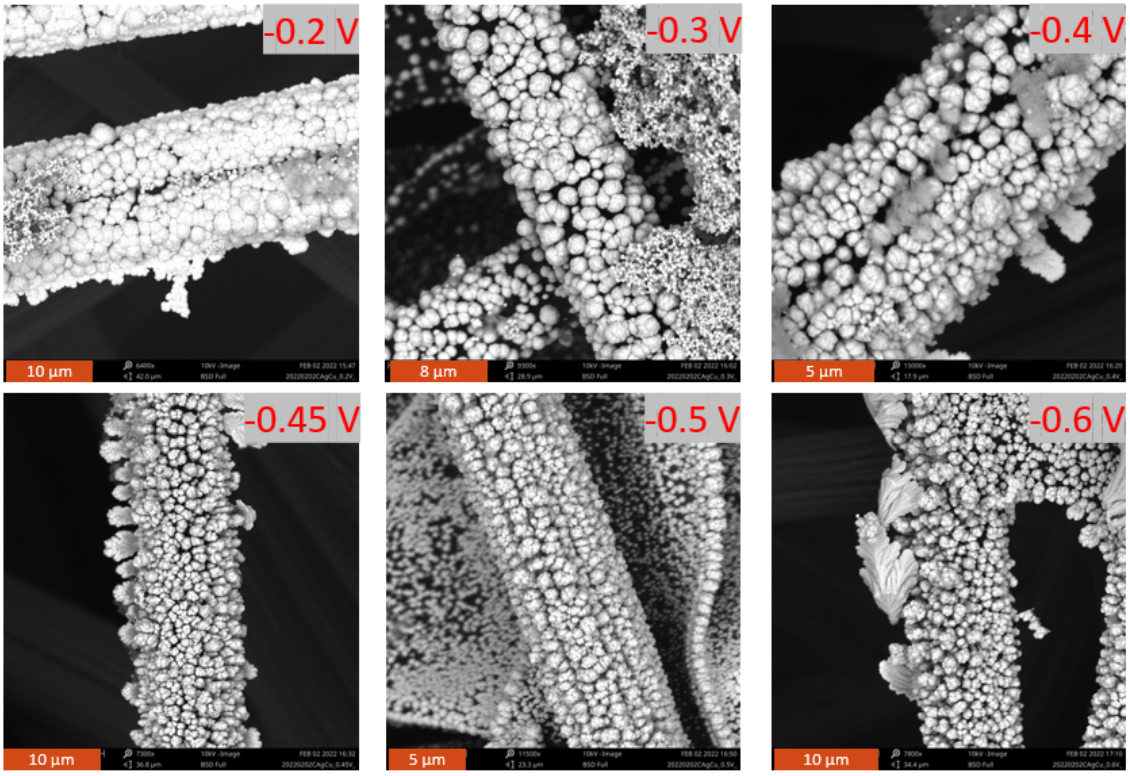

Figure A.10: SEM images of Ag/Cu deposited on carbon paper at potentials between 0.02 and -0.6 V vs Ag/AgCl.

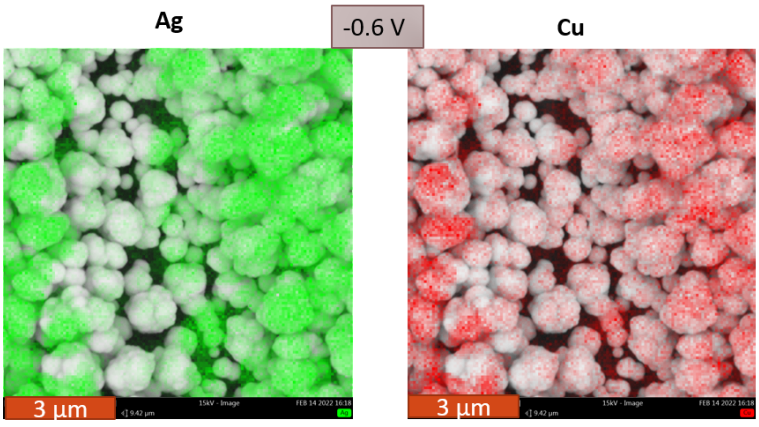

Figure A.11: EDX map of Ag and Cu on Ag/Cu codeposited at -0.6 V

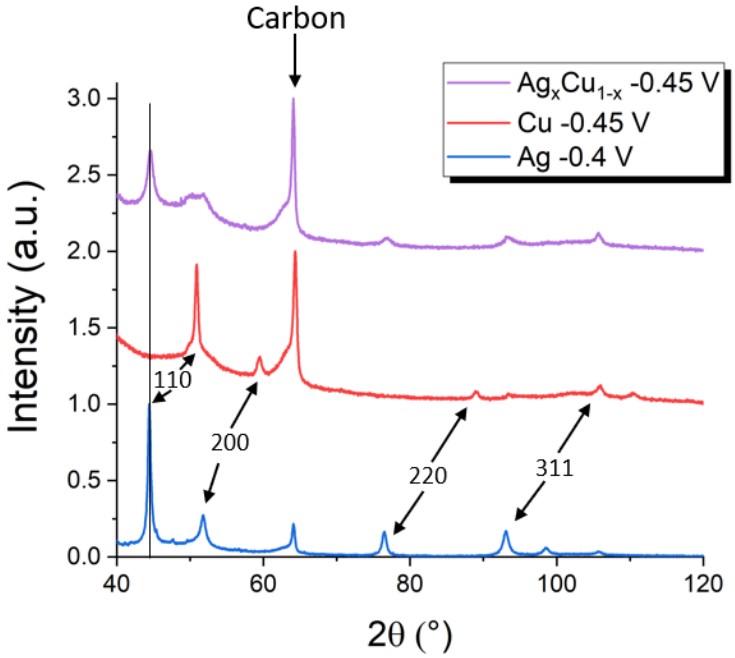

Figure A.12: XRD of Ag -0.4 V, Cu -0.45 V, and Ag/Cu -0.45 V.

Figure A.13: Picture of codeposited Ag-Cu on carbon paper.

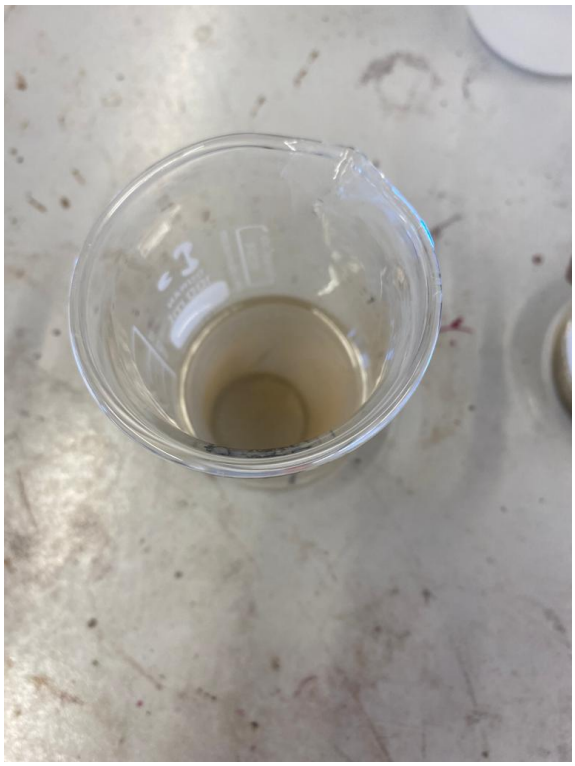

Figure A.14: Picture of codeposited Ag-Cu on carbon paper in acetone solution.

Solution	Motivation	Precipitation	Electrodeposition
Standard	Used in literature[49]	Yes	Ag/Cu codeposition possible, but also some spontaneous deposition, so not reproducible
1 M NH_4OH	Cu-NH_4OH complexes are soluble	No	Only Ag deposits, EDX does not detect Cu
0 M NH_4OH	Neutral pH so no precipitation	No, but spontaneous Ag formation causes the solution to turn into a gray suspension	Black, falls of the electrode. The remaining material is Ag/Cu
Halved amount of $AgNO_3$	According to Oliveira et al., the Ag/Cu ration should be below a certain value[49], and the standard solution was exactly that value	Yes	-
0.6125 M NH_4OH	Cu-NH_4OH complexes are soluble, 1 M NH_4OH was too much NH_4OH	No	Successful Ag/Cu codeposition

Table A.1: Attempted bath conditions for Ag/Cu codeposition

A.5 DLC

An example of how the C_{DL} is subtracted from DLC measurements is shown here. The raw data of the standard sample is shown in Figure A.15. As can be seen, it is a bit noisy, likely from the CO_2 bubbles that flow through the catholyte.

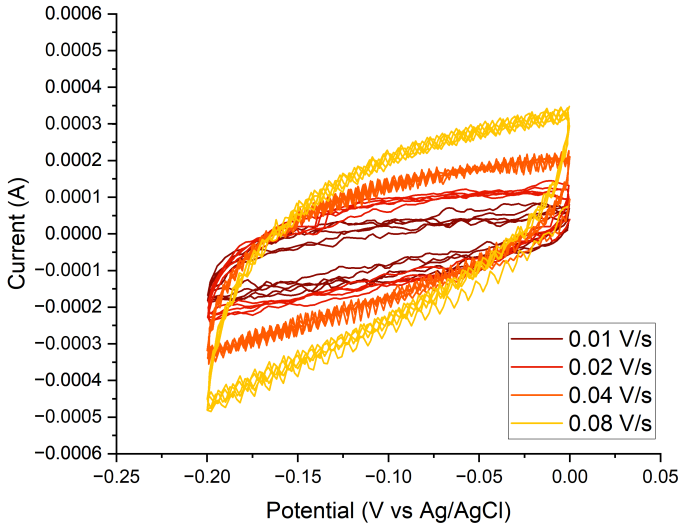

Figure A.15: Raw DLC data of standard sample

The average values from the last 3 cycles of the current in the middle of the potential window are plotted against the specific scan rate. A linear regression is fitted for the anodic and cathodic scans. The slope of this fit is C_{DL}, which in turn relates to the ECSA as described in Section 2.1.2.2.

As explained in the text, the data from the first scan rate (0.005 V/s) was discarded. However, especially for porous samples, this largely affected the ECSA. This shows how big errors in the analysis/measurement can be.

Table A.2: ECSA determined with DLC with and without first scan rate (0.005 V/s) for porous and non-porous catalysts .

Name	$ECSA_{porous}$ (cm^2) with	$ECSA_{porous}$ (cm^2) without	$ECSA_{non\text{-}porous}$ (cm^2) with	$ECSA_{non\text{-}porous}$ (cm^2) without
Standard	132.8	122.2	18.5	18.6
- 0.4 V	185.1	161.8	169.4	169
-5 mA	158.9	154.4	23.58	24.1
0.5 M $NaNO_3$	242.9	291.3	-	-
0 M EDTA	132.8	115.6	51.05	59
1 M NH_4OH	232	136.1	20.85	21.1

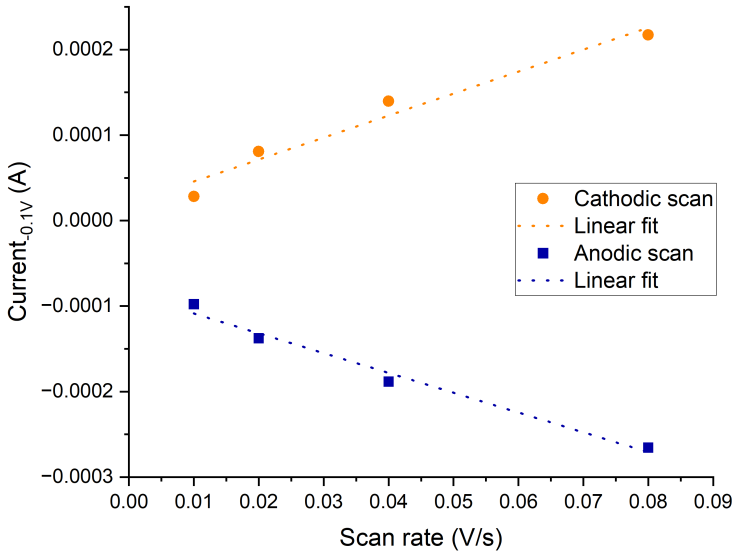

Figure A.16: Average current at -0.1 V vs Ag/AgCl plotted against scan rate with a linear fit for standard sample.

A.6 Size distribution PMMA and porous Ag

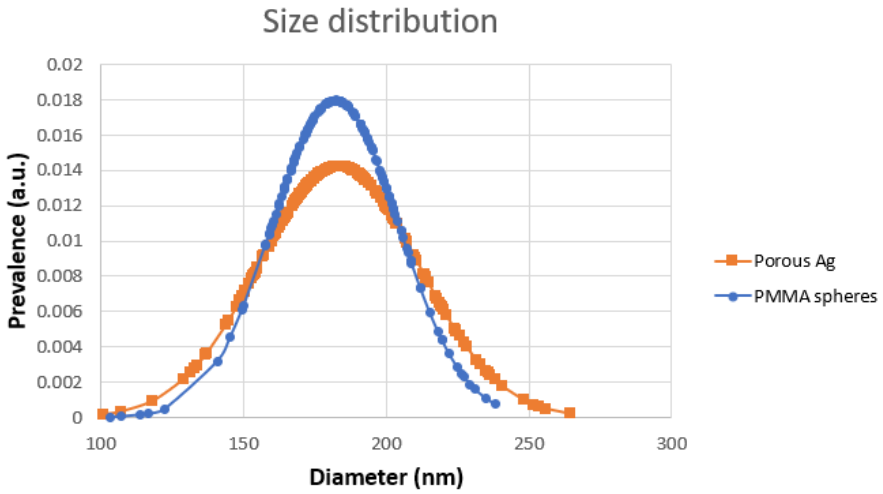

Figure A.17: Size distribution of PMMA spheres and pores in standard porous Ag

A.7 Other non-porous Ag samples

The HR-SEM images of non-porous Ag samples 0 M EDTA and 1 M NH_4OH are presented in Figures A.18 and A.19, respectively.

It is worth noting that the deposition of Ag on Ag foil without template did not occur homogeneously, as can be seen when compared to 0 M EDTA non-porous in

Figure A.20. Interestingly, the porous 1 M NH_4OH sample did have a normal Ag distribution.

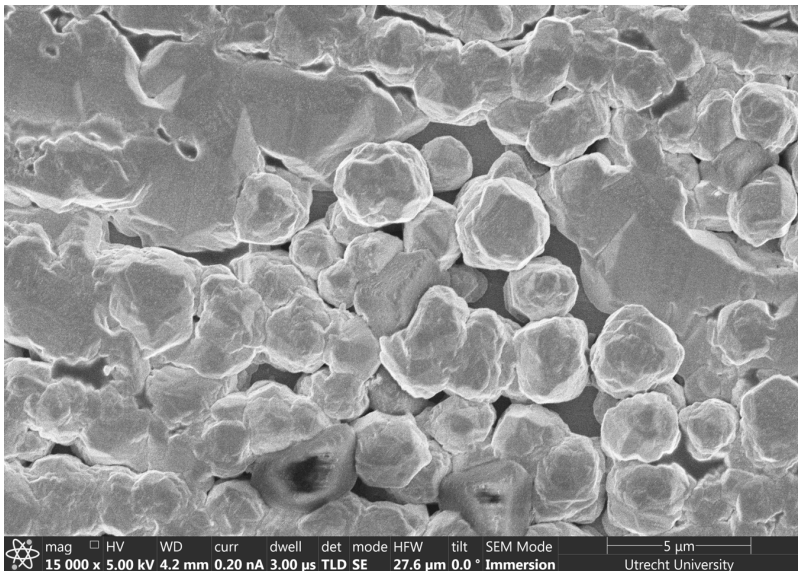

Figure A.18: HR-SEM image of non-porous 0 M EDTA sample

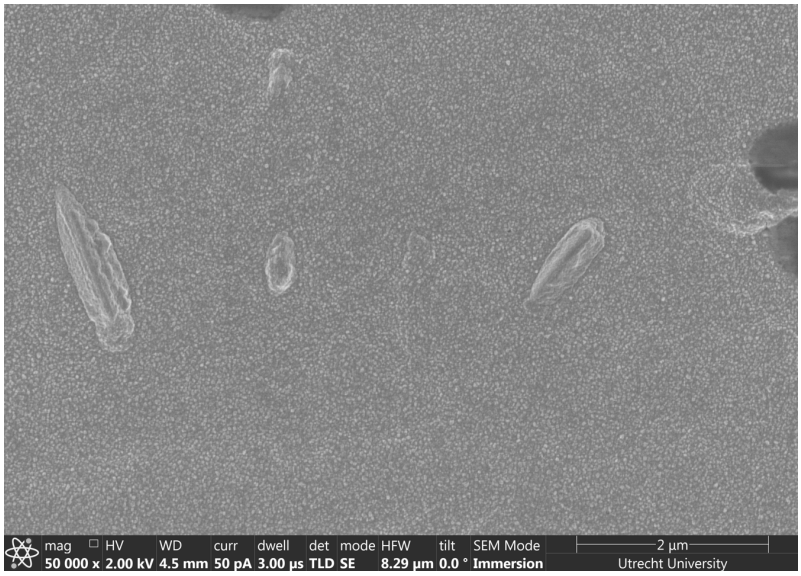

Figure A.19: HR-SEM image of non-porous 1 M NH_4OH sample

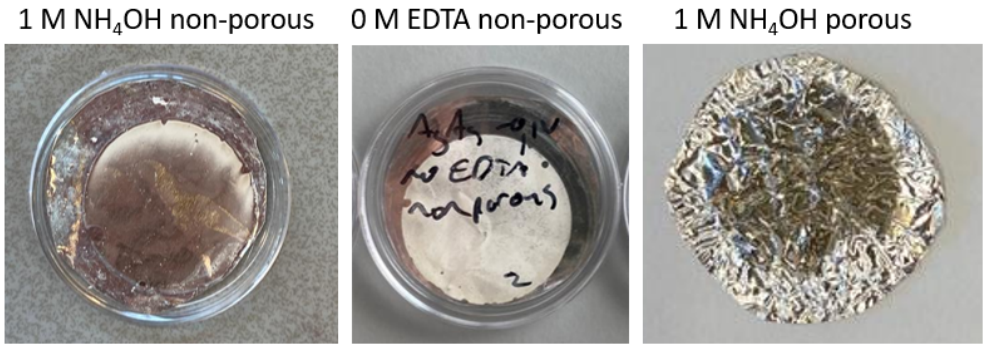

Figure A.20: Pictures of Ag deposited on Ag foil for 1 M NH_4OH non-porous and porous, and 0 M EDTA non-porous. Deposited non-porous silver has an very light grey color, and porous silver has a dark green colour..

A.8 A model of the expected increase in surface area

A model was built to simulate the increase in surface area by the PMMA template. The model starts with a box with sides x and y, and z. The surface on top of box A is given by

$$A = xy \tag{A.1}$$

The introduced pores are assumed to be spheres with diameter d. Each sphere has a surface area s of

$$s = 4\pi(0.5d)^2 \tag{A.2}$$

In 2D, the packing factor of the assumed fcc structure is equal to simple cubic. Therefore, the number of spheres that fit in one layer l can be described with.

$$l = xy/d^2 \tag{A.3}$$

The surface area for a layer of spheres A_{L} would therefore be

$$A_L = l * s \tag{A.4}$$

Using the equations above this can then be written as

$$A_L = xy/d^2 * 4\pi(0.5d)^2 \tag{A.5}$$

$$A_L = xy\pi \tag{A.6}$$

For top layer 1, it is assumed that the spheres are half spheres, as illustrated in Figure A.21. This ensures that the top layer is completely accessible. The surface area of layer 1 A_1 can then be described with

$$A_1 = 0.5 * xy\pi \tag{A.7}$$

When a new layer, layer 2, is introduced, we must take two things into account.

1) When 2 spheres touch, a hole appears in each sphere. This causes a loss of surface area. The model corrects for this by using a factor a. If a is 0.8, it means that each sphere loses 10% of its surface area.

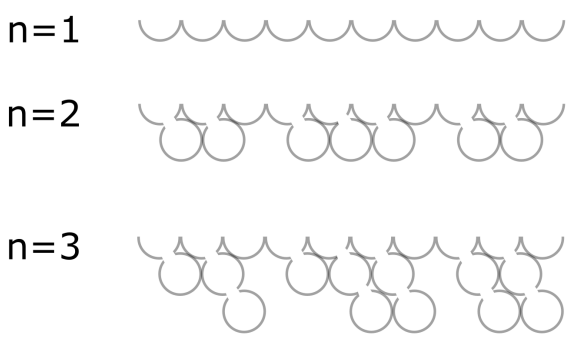

Figure A.21: Illustration of accessible pores for 1 to 3 layers. The grey line is the surface area that is included in the calculation.

2) Not all spheres in the new layer are accessible. This is corrected with factor b. If 70% of the spheres in layer 0 are in contact with layer one, b would be 0.7.

The surface area of layer 2 A_2 will therefore be

$$A_2 = abxy\pi \tag{A.8}$$

For the next layer, layer 3, an extra factor b is necessary to again compensate for the loss of the new layer. The surface area of layer 3 A_3 can therefore be described by

$$A_3 = ab^2xy\pi \tag{A.9}$$

And so on and on, which means that the surface area of layer n A_n can be described by

$$A_n = ab^{n-1}xy\pi \tag{A.10}$$

The total surface area of the porous structure A_p will be a summation of all of these layers. The maximum amount of layers n_max in the box can be described

$$n_{max} = z/d \tag{A.11}$$

So for

$$n \leq n_{max}$$

A_p will be

$$A_p = (0.5 + \sum_{k=1}^{n-1} ab^{n-1})xy\pi \tag{A.12}$$

The surface area of the porous structure A_p will be bigger than the original surface area A by a factor of F

$$F = A_p/A \tag{A.13}$$

$$F = (0.5 + \sum_{k=1}^{n-1} ab^{n-1})\pi \tag{A.14}$$

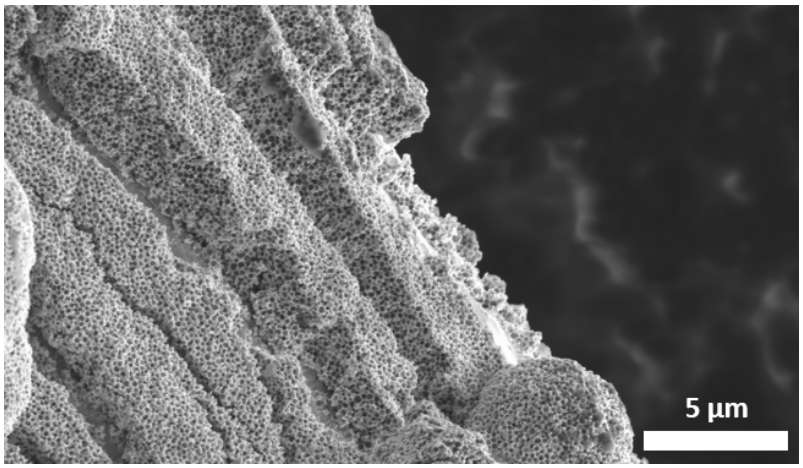

Figure A.22: HR-SEM image of porous -0.1 V, allowing an estimation for the number of pore layers.

A.9 Ag foil

When comparing the j_{CO} values of Standard porous Ag to Ag foil, j_{CO} increases with a factor 16.2 at - 0.7 V vs RHE, or 1.75 at -1.4 V vs RHE.

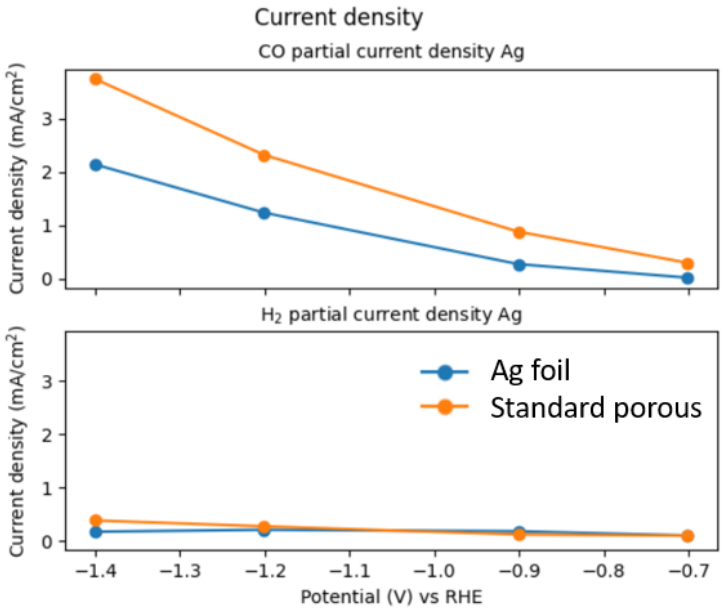

Figure A.23: CO and H_2 partial current densities of Ag foil and Standard porous Ag.

A.10 Inhomogeneity porous Ag

Interestingly, the color of deposited Ag changes upon changing morphology. On a porous catalyst, the dark regions are porous, whereas the light regions are non-porous, as confirmed by SEM. In Figure A.24, it can be seen that there can be a significant amount of non-porous regions on a porous Ag catalyst.

Figure A.24: Pictures of 2 porous Ag catalysts. The dark regions are porous, and the light regions are non-porous

Figure A.25 shows an HR-SEM image of a porous Ag catalyst in a region that contains both a porous and non-porous silver. It seems like there is a porous layer under the non-porous layer, which means that overgrowth occurred and the PMMA layer was not thick enough in this region.

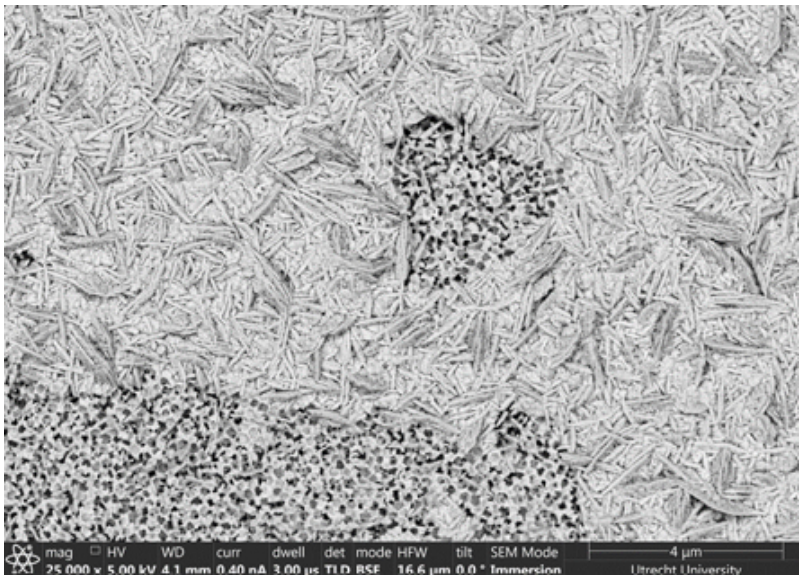

Figure A.25: HR-SEM of porous Ag, showing porous and non-porous regions at the same time.

A.11 Intrinsic activity

The intrinsic catalytic activity was determined by normalizing the partial current densities to the electrochemical surface areas instead of the geometric surface area. As becomes clear in Figure A.26, Ag foil shows the highest intrinsic activity, then the non-porous samples (excluding -0.4 V, which has a very high ECSA), and lastly the porous samples and -0.4 V non-porous. Note that -0.1 V corresponds to the standard sample.

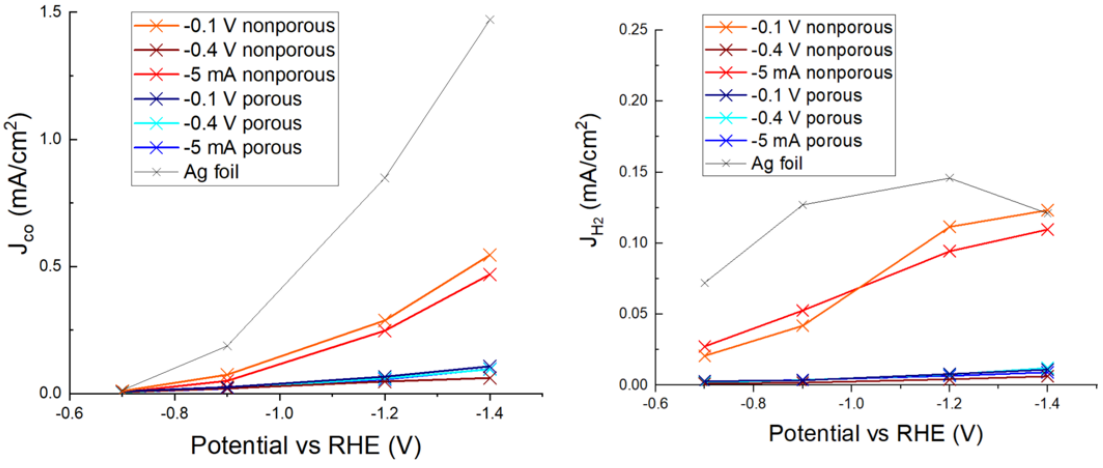

Figure A.26: CO and H_2 partial current densities normalized by electrochemical surface area.

A.12 Reproducibility

For the porous 0.5 M $NaNO_3$ sample, a reproducibility experiment was performed. Two different samples were tested for catalysis. The resulting j_{CO} and j_{H2} can be found in Figure A.27. The j_{CO} value is very constant, with only a difference of 0.13 mA/cm^2 between the two samples. However, the difference in j_{H2} has a more significant value of 0.4 mA/cm^2. It should be noted that there were some differences between these two experiments. Most importantly, they were performed in different electrochemical cells. In addition, for sample 1 the polishing in the diamond suspension was not performed in the right order, and after 2 days, the electrolyte was gone, which might imply that there was a small leak. However, due to the high activity of porous silver, and the short time of the catalytic measurement, it is expected that the latter 2 factors have not contributed significantly to the differences in partial current densities.

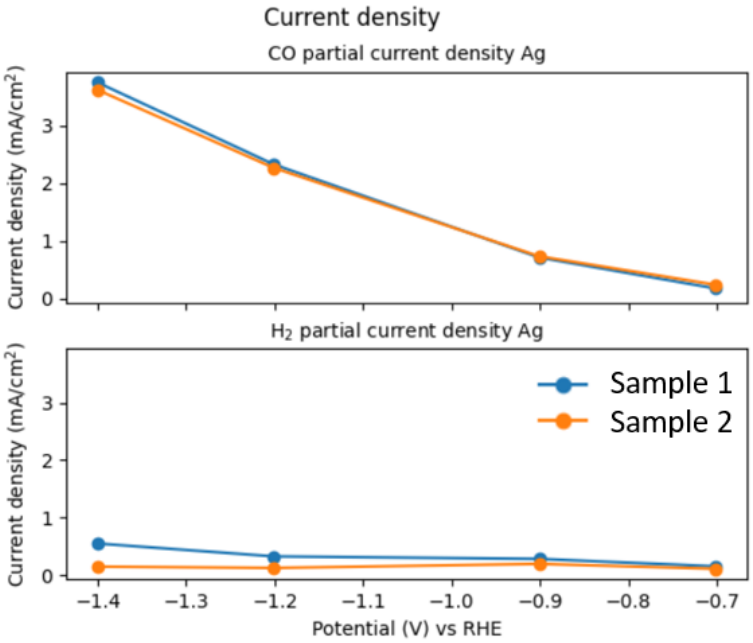

Figure A.27: CO and H_2 partial current densities of two different porous 0.5 M $NaNO_3$ samples.

A.13 Low overpotentials

The catalytic performance of Ag foil and porous Ag were tested at less negative potentials (-1.1, -1.2, -1.3, -1.4 V vs Ag/AgCl instead of -1.3, -1.5, -1.8, -2.0 V vs Ag/AgCl). As can be seen in Figure A.28, high missing faradaic efficiencies were encountered at these potentials. In addition, the CO partial current density of porous Ag is 23 times as high as Ag foil at -1.3 V vs Ag/AgCl.

	Ag foil						Ag porous				
Potential (V) vs Ag/AgCl)	CO FE (%)	H_2 FE (%)	missing FE (%)	CO pcd (mA/cm²)	H_2 pcd (mA/cm²)		CO FE (%)	H_2 FE (%)	missing FE (%)	CO pcd (mA/cm²)	H_2 pcd (mA/cm²)
-1.1	0	0	100	0	0		13.19102	0	86.80898	0.011045	0
-1.2	0	53.12943	46.87057	0	0.05562		35.1378	28.09605	36.76616	0.06956	0.05562
-1.3	3.08387	77.64962	19.26651	0.007179	0.180765		42.58998	17.8303	39.57972	0.166069	0.069525
-1.4	1.832982	13.70111	84.46591	0.039065	0.292005		19.28764	2.643563	78.06879	0.405807	0.05562

Figure A.28: Table of CO, H_2, and missing faradaic efficiencies and CO and H_2 partial current densities at -1.1, -1.2, -1.3, -1.4 V vs Ag/AgCl

A.14 Residual PMMA

Interestingly, performing EDX on the Ag samples revealed that the porous silver samples contained carbon, however, this depended on the SEM (Figure A.29). It could be that the Ag and C peaks overlap, but also that residual PMMA was present. The EVO-15 allowed peak deconvolution (Figure A.30) and doing this for porous

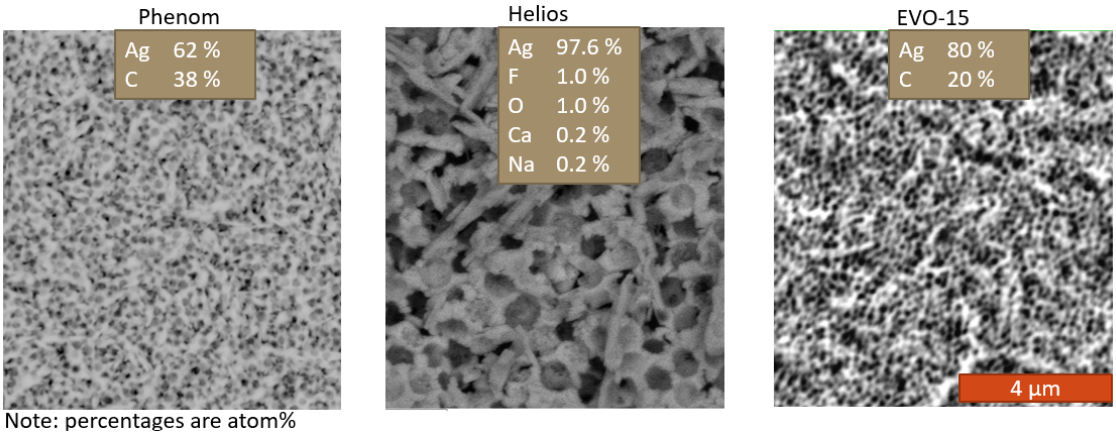

Figure A.29: EDX on porous Ag from 3 different scanning electron microscopes.

Ag and Ag foil demonstrated that the apparent C is partially a result of overlapping peaks, but also from residual PMMA.

Immersion of PMMA in HNO_3 demonstrated that PMMA does not dissolve in it, unlike Ag, but merely turns more transparent and viscous. The presence of residual PMMA was confirmed by dissolving a porous Ag sample in concentrated HNO_3 (Figure A.31). A cloudy substance appeared above the sample while the silver was dissolving, which was attributed to PMMA.

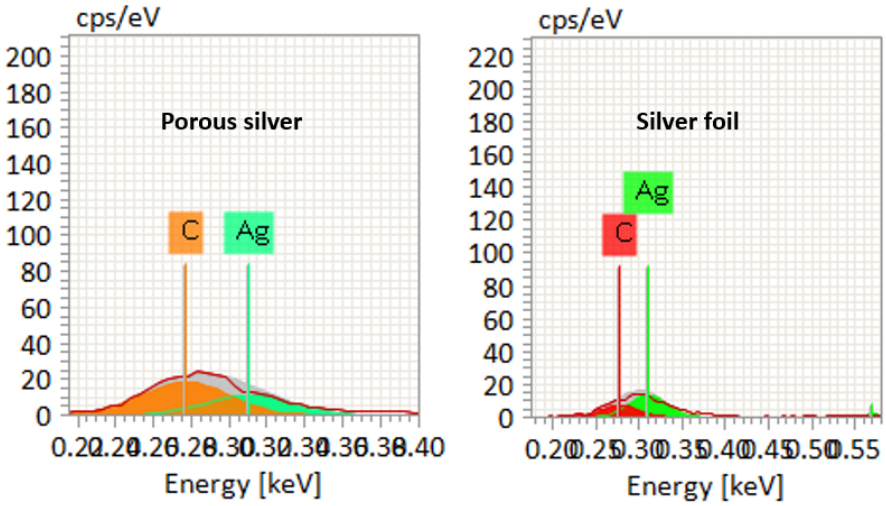

Figure A.30: EDX peak deconvolution of porous Ag and Ag foil.

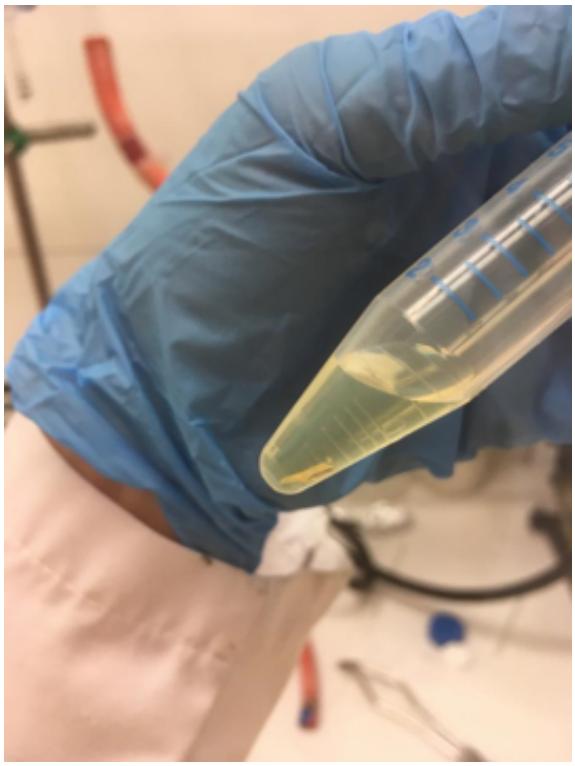

Figure A.31: Porous Ag dissolved in concentrated HNO_3

A.15 Effect of PMMA layer thickness

For one standard sample, a second layer of PMMA was applied after drying the first PMMA layer, in order to investigate the effect of PMMA layer thickness. Interestingly, in regions where the PMMA layer was too thick, no Ag deposition occurred. As a result, the ECSA of the sample with 2 layers (96 cm^2) was smaller than the sample with one PMMA layer (122 cm^2). This also affected the catalytic performance, as seen in Figure A.32. A thicker layer leads to a lower j_{CO} and j_{H2}.

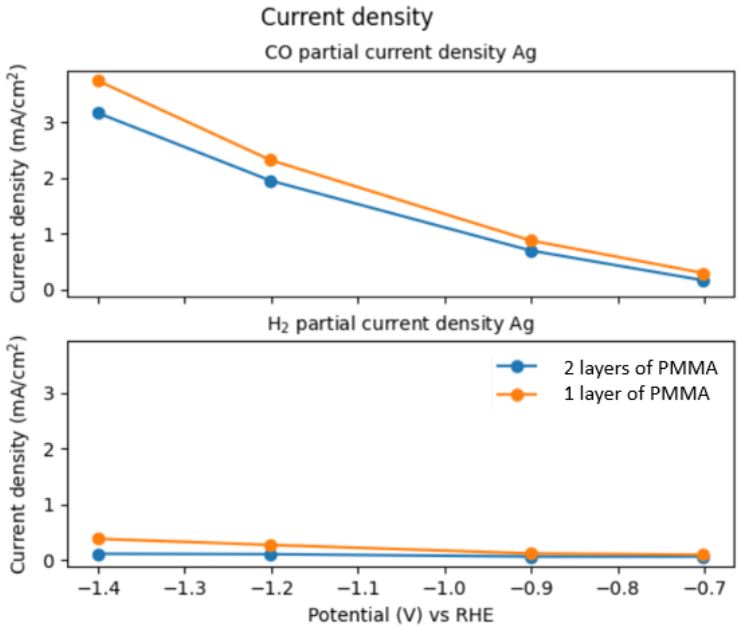

Figure A.32: CO and H_2 partial current densities for 1 or 2 layers of PMMA.

Appendix B

List of samples

Name sample	Date	Metal	Solution	Potential
Agfx	08/12/2021	Ag	Standard	-5 mA
Agfx2	08/12/2021	Ag	Standard	-5 mA
AgAgCu	15/02/2022	Ag+Cu	1 M ammonia	-0.4 V
AgAg-0.1V1	21/04/2022	Ag	Standard	-0.1 V
AgAg-0.1V2	21/04/2022	Ag	Standard	-0.1 V
AgAg-0.1V3	21/04/2022	Ag	Standard	-0.1 V
AgAg-0.4V1	29/04/2022	Ag	Standard	-0.4 V
AgAg-0.4V2	29/04/2022	Ag	Standard	-0.4 V
AgAg-0.4V3	29/04/2022	Ag	Standard	-0.4 V
AgAg-0.4V0Mammonia	22/07/2022	Ag	0 M ammonia	-0.4 V
AgAg-0.1VnoEDTA nonporeus1	29/07/2022	Ag	no EDTA	-0.1 V
AgAg-0.1VnoEDTA nonporeus2	29/07/2022	Ag	no EDTA	-0.1 V
AgAg-0.1VnoEDTA nonporeus3	29/07/2022	Ag	no EDTA	-0.1 V
AgAg-0.1VnoEDTA nonporeus4	29/07/2022	Ag	no EDTA	-0.1 V
AgAg-0.1V1Mam nonporeus1	04/08/2022	Ag	1M ammonia	-0.1 V
AgAg-0.1V1Mam nonporeus2	04/08/2022	Ag	1M ammonia	-0.1 V
AgAg-0.1V1Mam nonporeus3	04/08/2022	Ag	1M ammonia	-0.1 V

Table B.1: List of non-porous samples on Ag foil

Name sample	Date	Metal	Binder	Bath	Potential
Agn1/Agfn1/ Agfxn1	08/12/2021	Ag	Nafion	Standard	-5 mA
Agn2/Agfn2	13/12/2021	Ag	Nafion	Standard	-5 mA
Agn3/Agfn3	13/12/2021	Ag	Nafion	Standard	-5 mA
Agfneg1	12/01/2022	Ag	Nafion	Standard	-5 mA
Agfndg1	12/01/2022	Ag	Nafion	Standard	-5 mA
Agfndg2	12/01/2022	Ag	Nafion	Standard	-5 mA
Agfpeg1	12/01/2022	Ag	P123	Standard	-5 mA
Agfpeg2	12/01/2022	Ag	P124	Standard	-5 mA
Agfpdg1	12/01/2022	Ag	P125	Standard	-5 mA
Agfpdg2	12/01/2022	Ag	P126	Standard	-5 mA
AgAgCun	15/02/2022	Ag+Cu	nafion	1 M ammonia	-0.4 V
AgAg-0.1VPMMA1	21/04/2022	Ag	Nafion	Standard	-0.1 V
AgAg-0.1VPMMA2	21/04/2022	Ag	Nafion	Standard	-0.1 V
AgAg-0.1VPMMA3	21/04/2022	Ag	Nafion	Standard	-0.1 V
AgAg-0.4VPMMA1	29/04/2022	Ag	nafion	Standard	-0.4 V
AgAg-0.4VPMMA2	29/04/2022	Ag	nafion	Standard	-0.4 V
AgAg-0.4VPMMA3	29/04/2022	Ag	nafion	Standard	-0.4 V
AgAg-0.4VPMMAhalf	29/04/2022	Ag	nafion	Standard	-0.4 V
AgAg-0.1VPMMAdun1	30/05/2022	Ag	nafion	Standard	-0.1 V
AgAg-0.1VPMMAdun2	30/05/2022	Ag	nafion	Standard	-0.1 V
AgAg-0.1VnoEDTA poreus1	29/07/2022	Ag	nafion	no EDTA	-0.1 V
AgAg-0.1VnoEDTA poreus2	29/07/2022	Ag	nafion	no EDTA	-0.1 V
AgAg-0.1VnoEDTA poreus3	29/07/2022	Ag	nafion	no EDTA	-0.1 V
AgAg-0.1V1Mamporeus1	04/08/2022	Ag	nafion	1M ammonia	-0.1 V
AgAg-0.1V1Mamporeus2	04/08/2022	Ag	nafion	1M ammonia	-0.1 V
AgAg-0.1V1Mamporeus3	04/08/2022	Ag	nafion	1M ammonia	-0.1 V

Table B.2: List of porous samples on Ag foil - part 1

Name sample	Date	Metal	Binder	Bath	Potential
Ag-Cu-por1	08/09/2022	Cu	nafion	0.6125 M ammonia	-0.5 V
Ag-Cu-por2	08/09/2022	Cu	nafion	0.6125 M ammonia	-0.5 V
Ag-CuAgpor1	08/09/2022	Cu layer, Ag layer	nafion	0.6125 M ammonia Cu, Standard Ag	-0.5 V Cu, -0.2V Ag
Ag-CuAgpor2	08/09/2022	Cu layer, Ag layer	nafion	0.6125 M ammonia Cu, Standard Ag	-0.5 V Cu, -0.2V Ag
Ag-CuAgpor3	08/09/2022	Cu layer, Ag layer	nafion	0.6125 M ammonia Cu, Standard Ag	-0.5 V Cu, -0.2V Ag
Ag-AgCupor1	08/09/2022	Ag layer, Cu layer	nafion	0.6125 M ammonia Cu, Standard Ag	-0.5 V Cu, -0.2V Ag
Ag-AgCupor2	08/09/2022	Ag layer, Cu layer	nafion	0.6125 M ammonia Cu, Standard Ag	-0.5 V Cu, -0.2V Ag
AgAg-0.1V0.5NaNO31	15/09/2022	Ag	nafion	0.5 M NaNO3	-0.1 V
AgAg-0.1V0.5NaNO32	15/09/2022	Ag	nafion	0.5 M NaNO3	-0.1 V
AgAg-0.1V0.5NaNO33	15/09/2022	Ag	nafion	0.5 M NaNO3	-0.1 V
AgAg-0.1V0.5NaNO34	15/09/2022	Ag	nafion	0.5 M NaNO3	-0.1 V
AgAg-0.1V0.5NaNO3half	15/09/2022	Ag	nafion	0.5 M NaNO3	-0.1 V
AgCulaagpor	15/09/2022	Ag layer, thin Cu layer	nafion	0.6125 M ammonia Cu, Standard Ag	-0.5 V Cu, -0.2V Ag
AgCucodeppor	15/09/2022	Ag+Cu	nafion	0.6125 M ammonia, half Ag	-0.5 V
Ag-AgCu0.5_laag_1	06/10/2022	Ag+Cu	nafion	0.6125 M ammonia Cu, Standard Ag	-0.5 V Cu, -0.2V Ag
Ag-AgCu0.5_laag_2	06/10/2022	Ag+Cu	nafion	0.6125 M ammonia Cu, Standard Ag	-0.5 V Cu, -0.2V Ag
Ag-AgCu0.5_laag_3	06/10/2022	Ag+Cu	nafion	0.6125 M ammonia Cu, Standard Ag	-0.5 V Cu, -0.2V Ag

Table B.3: List of porous samples on Ag foil - part 2

Name sample	Date	Metal	Bath	Potential
CPtest3/CAg	01/12/2021	Ag	Standard	-5ma
CAg0.1V1	20/01/2022	Ag	Standard	-0.1 V
CAg0.1V2	20/01/2022	Ag	Standard	-0.1 V
CAg0.01V	20/01/2022	Ag	Standard	-0.01 V
Cag-0.05V	20/01/2022	Ag	Standard	0.05V
CAg0.2V	20/01/2022	Ag	Standard	-0.2 V
CAg0.4V	20/01/2022	Ag	Standard	-0.4 V
CAg0.6V	21/01/2022	Ag	Standard	- 0.6 V
CCu0.38V	28/01/2022	Cu	Standard	-0.38 V
CCu0.4V	28/01/2022	Cu	Standard	-0.4 V
CCu0.45V	28/01/2022	Cu	Standard	-0.45 V
CCu0.5V	28/01/2022	Cu	Standard	-0.5 V
CCu0.55V	28/01/2022	Cu	Standard	-0.55 V
CCu0.6V	28/01/2022	Cu	Standard	-0.6 V
CAgCu0.2V	02/02/2022	Ag+Cu	Standard	-0.2 V
CAgCu0.3V	02/02/2022	Ag+Cu	Standard	-0.3 V
CAgCu0.4V	02/02/2022	Ag+Cu	Standard	-0.4 V
CAgCu0.5V	02/02/2022	Ag+Cu	Standard	-0.5 V
CAgCu0.6V	02/02/2022	Ag+Cu	Standard	-0.6 V
CAgCu0.65V	02/02/2022	Ag+Cu	Standard	-0.65 V
CAgCu0.45V	02/02/2022	Ag+Cu	Standard	-0.45 V
CAgCuam0.1V	15/02/2022	Ag+Cu	1 M ammonia	-0.1 V
CAgCuam0.2V	15/02/2022	Ag+Cu	1 M ammonia	-0.2 V
CAgCuam0.3V	15/02/2022	Ag+Cu	1 M ammonia	-0.3 V
CAgCuam0.4V	15/02/2022	Ag+Cu	1 M ammonia	-0.4 V
CAgCuam0.5V	15/02/2022	Ag+Cu	1 M ammonia	-0.5 V
CAgCuam0.6V	15/02/2022	Ag+Cu	1 M ammonia	-0.6 V
CAgCuam0.4V	15/02/2022	Ag+Cu	1 M ammonia	-0.4 V
CCu0.65V1M	01/04/2022	Cu	1 M ammonia	-0.65 V
CCu0.65V1Mroer	01/04/2022	Cu	1 M ammonia	-0.65 V
CCu0.7V1M	01/04/2022	Cu	1 M ammonia	-0.7 V
CCu0.7V1M2	01/04/2022	Cu	1 M ammonia	-0.7 V
CCu0.8V1M	01/04/2022	Cu	1 M ammonia	-0.8 V
CCu1V1M	01/04/2022	Cu	1 M ammonia, 0.02 M EDTA	-1 V
CCu0.7V1MEDTA	01/04/2022	Cu	1 M ammonia	-0.7 V
CAgCu-0.6V_noam	08/04/2022	Ag+Cu	0M ammonia	-0.6V
CAgCu-0.8V_noam	08/04/2022	Ag+Cu	0M ammonia	-0.8V
CAgCu-1V_noam	08/04/2022	Ag+Cu	0M ammonia	-1V
CAgCu-0.4V_noam	08/04/2022	Ag+Cu	0M ammonia	-0.4V

Table B.4: List of non-porous samples on carbon paper - part 1

Name sample	Date	Metal	Bath	Potential
CAg-0.1VnoEDTA	26/07/2022	Ag	no EDTA	-0.1 V
CAg-0.1V1/2NaNO3	27/07/2022	Ag	0.5 M NaNO3	-0.1 V
CAg-0.1VnoEDTA non-porous	29/07/2022	Ag	no EDTA	-0.1 V
CAg-0.1V1Mam non-poreus1	04/08/2022	Ag	1M ammonia	-0.1 V
CAgCu-0.4V non-poreus1	11/08/2022	Ag+Cu	Standard	-0.4 V
CAgCu-0.4V non-poreus2	11/08/2022	Ag+Cu	Standard	-0.4 V
CAgCu-0.4V non-poreus3	11/08/2022	Ag+Cu	Standard	-0.4 V
CAgCu-0.4V non-poreus4	11/08/2022	Ag+Cu	Standard	-0.4 V
CAgCu-0.5V 0.6am0.5Ag1	02/09/2022	Ag+Cu	0.6125 M ammonia, half Ag	-0.5 V
CAgCu-0.5V 0.6am0.5Ag2	02/09/2022	Ag+Cu	0.6125 M ammonia, half Ag	-0.5 V
CAgCu-0.5V 0.6am0.5Ag3	02/09/2022	Ag+Cu	0.6125 M ammonia, half Ag	-0.5 V

Table B.5: List of non-porous samples on carbon paper - part 2

Name sample	Date	Metal	Binder	Bath	Potential
CPtest1	29/11/2021	Ag	No	Standard	-5 mA
CPtest2	30/11/2021	Ag	No	Standard	-5 mA
CAgCun1	16/02/2022	Ag+Cu	nafion	1 M ammonia	-0.4 V
CAgCun2	17/02/2022	Ag+Cu	nafion	1 M ammonia	-0.4 V
CAg-0.1VnoEDTA porous	29/07/2022	Ag	No	no EDTA	-0.1 V
CAg-0.1V1Mamporeus1	04/08/2022	Ag	No	1M ammonia	-0.1 V
CAgCu-0.4Vpmma1	11/08/2022	Ag+Cu	nafion	Standard	-0.4 V
CAgCu-0.4Vpmma2	11/08/2022	Ag+Cu	nafion	Standard	-0.4 V
CAgCu-0.4Vpmma3	11/08/2022	Ag+Cu	nafion	Standard	-0.4 V
CAgCu-0.5V0.6am 0.5Agporeus1	02/09/2022	Ag+Cu	Nafion	0.6125 M ammonia, half Ag	-0.5 V
CAgCu-0.5V0.6am 0.5Agporeus2	02/09/2022	Ag+Cu	Nafion	0.6125 M ammonia, half Ag	-0.5 V
CAgCu-0.5V0.6am 0.5Agporeus3	02/09/2022	Ag+Cu	Nafion	0.6125 M ammonia, half Ag	-0.5 V

Table B.6: List of porous samples on carbon paper